HOSTED BY
ELSEVIER
Available online at www.sciencedirect.com
ScienceDirect
Soils and Foundations 66 (2026) 101868
www.elsevier.com/locate/sandf

Technical Paper

Comprehensive analysis of pumice sand: physical, chemical, and mechanical behavior under static and cyclic triaxial testing

I Wayan Ariyana Basoka [a,b,*], Kiyonobu Kasama [b], Zentaro Furukawa [c], Noriyuki Yasufuku [d], Ahmad Rifa'i [e]

[a] Department of Civil Enginering, Universitas Warmadewa, Bali, Indonesia
[b] Department of Civil Engineering, Kyushu University, Fukuoka, Japan
[c] Faculty of Environmental and Life Science, Okayama University, Okayama, Japan
[d] Kyushu Infrastructure Management Association, Fukuoka, Japan
[e] Department of Civil and Environmental Engineering, Universitas Gadjah Mada, Yogyakarta, Indonesia

Received 5 December 2025; received in revised form 4 August 2026; accepted 15 August 2026
Available online 7 September 2026

Abstract

Pumice sand is a highly porous and crushable volcanic soil widely distributed in volcanic regions such as Japan, where it may contribute to earthquake-induced ground deformation, liquefaction, and slope instability. However, the coupled effects of particle crushability, density, and confining pressure on its monotonic and cyclic behavior remain insufficiently clarified, resulting in uncertainty in geotechnical design for volcanic deposits. This study investigates the mechanical characteristics and liquefaction resistance of pumice sand obtained from Miyakonojo City, Miyazaki Prefecture, Kyushu, Japan. A comprehensive laboratory testing program was conducted, including chemical analysis, single-particle strength tests, one-dimensional consolidation compression tests, static and cyclic triaxial tests. The results show that the tested pumice sand is predominantly composed of silica (SiO_2) and has considerably lower particle strength than conventional sands such as Toyoura sand and carbonate sand, confirming its highly crushable nature. The consolidation response indicates a yield stress intermediate between typical sand and clay-like behavior, reflecting the influence of its porous particle structure. Static triaxial tests reveal that particle crushing is more pronounced under drained conditions than under undrained conditions. Cyclic triaxial tests further demonstrate that liquefaction resistance is governed by relative density and confining pressure, with denser specimens requiring a greater number of loading cycles to reach liquefaction. In addition, lower confining pressure results in higher apparent liquefaction resistance, which may be attributed to reduced particle crushing during cyclic loading. These findings clarify the distinctive mechanical response of pumice sand and provide an experimental basis for improving liquefaction assessment and geotechnical design in volcanic regions.
© 2026 Japanese Geotechnical Society. Published by Elsevier B.V. This is an open access article under the CC BY license (http://creativecommons.org/licenses/by/4.0/).

Keywords: Pumice; Single particle; Static triaxial; Cyclic triaxial; Liquefaction

1. Introduction

Japan is one of the most volcanically active regions in the world, resulting in the widespread distribution of volcanic soils that often pose significant geotechnical challenges. These deposits are frequently associated with earthquake-induced slope failures, ground deformation, and liquefaction. Among volcanic geomaterials, pumice is commonly encountered as a pyroclastic deposit produced during explosive eruptions (Fisher, 1961; McPhie et al.,

* Corresponding author at: Department of Civil Engineering, Warmadewa University Indonesia.
E-mail address: basokaariyana@warmadewa.ac.id (I Wayan Ariyana Basoka).

https://doi.org/10.1016/j.sandf.2026.101868
0038-0806/© 2026 Japanese Geotechnical Society. Published by Elsevier B.V.
This is an open access article under the CC BY license (http://creativecommons.org/licenses/by/4.0/).

1993). Owing to its highly porous vesicular structure, pumice generally exhibits low particle strength, high compressibility, and pronounced crushability. These intrinsic characteristics can strongly affect its stress–strain response, volumetric behavior, pore pressure generation, and cyclic resistance, making pumice sand an important material to evaluate in seismic geotechnical design.

Geotechnical failures associated with pumiceous deposits and volcanic soils have been reported in several regions, including Indonesia, Japan, New Zealand, and the United States (Chiaro et al., 2022; Crosta et al., 2005; Faris and Fawu, 2014; Hazarika et al., 2019; Hosobuchi et al., 2021; Kasama et al., 2021; Siebe et al., 2017; Sumartini et al., 2018). A notable example is the Takanodai landslide triggered by the 2016 Kumamoto earthquake, the failure occurred on a relatively gentle slope of approximately 15° and caused substantial ground displacement and damage to residential structures. Previous investigations suggested that the presence of a weak pumice layer played an important role in the initiation and development of the failure mechanism (Chiaro et al., 2022; Hazarika et al., 2019; Kasama et al., 2021; Sumartini et al., 2018; Umar et al., 2018).

The geological profile reported by Kasama et al. (2021), shown in Fig. 1, identified a thin pumice layer at a depth of approximately 9.30–9.40 m. The particle strength of this pumice layer was significantly lower than that of carbonate sand and much lower than that of silica sand such as Toyoura sand. This suggests that pumice-rich layers may act as potential weak zones in volcanic soil deposits, reducing shear resistance and promoting instability during seismic loading. Previous studies have examined the mechanical response and liquefaction behavior of pumice and other crushable soils. Orense and Pender (2013) demonstrated that pumice exhibits liquefaction characteristics distinct from those of hard-grained sands, indicating that conventional empirical approaches developed for silica sands may not be directly applicable. Faris and Fawu (2014) and Asadi et al. (2022) further showed that confining pressure, density, and particle characteristics strongly influence pore pressure development and cyclic resistance. In parallel, studies on particle crushing have emphasized the role of particle strength, morphology, and breakage potential in controlling the macroscopic behavior of granular materials (Bengtsson, 2021; He et al., 2022; Kwag et al., 1999; Nakata et al., 2001; Yoshimoto et al., 2012).

Despite these advances, the relationship between particle-scale characteristics and the macro-scale mechanical and liquefaction behavior of pumice sand remains insufficiently understood. In particular, limited experimental evidence is available on how the low particle strength and high crushability of pumice influence its drained, undrained, and cyclic response under different density and confining pressure conditions. Moreover, pumice

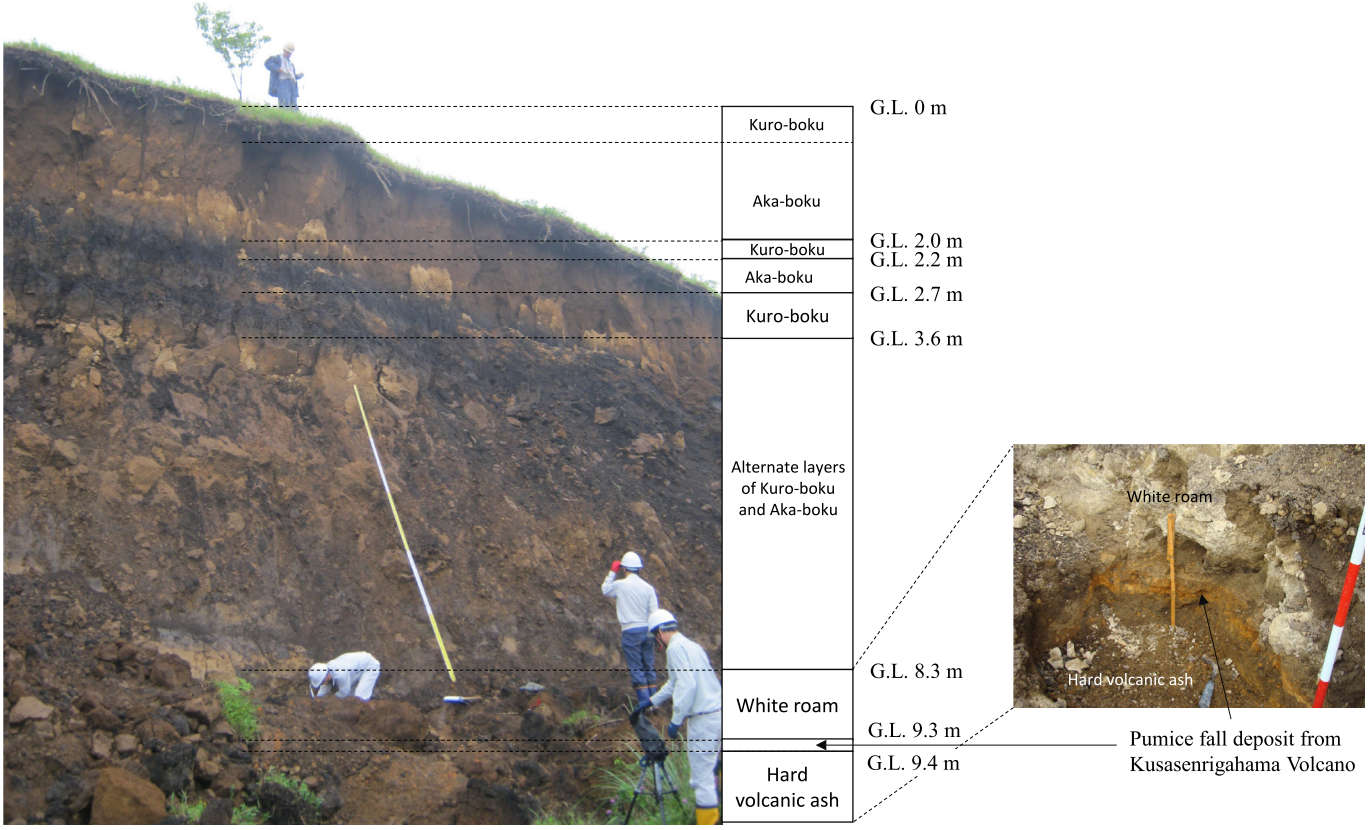

Fig. 1. Geological condition at Takanodai landslide 2016 (Kasama et al., 2021).

deposits from Kyushu, Japan, have not been extensively investigated, despite their relevance to earthquake-induced ground failures in volcanic regions. To address these limitations, this study investigates the mechanical and liquefaction behavior of pumice sand obtained from Miyakonojo City, Miyazaki Prefecture, Kyushu, Japan. The study integrates particle-scale strength characterization with macro-scale laboratory testing, including single-particle strength tests, one-dimensional consolidation compression tests, and drained, undrained, and cyclic triaxial tests. The combined effects of density, confining pressure, and particle crushing on liquefaction resistance are systematically evaluated to provide a clearer experimental basis for geotechnical design in volcanic soil deposits (Shen et al., 2016).

2. Material

The pumice samples were collected from adjacent regions of Miyakonojo City, Miyazaki Prefecture, Kyushu Island, Japan, as shown in Fig. 2. Pumice samples are acquired from firms collecting pumice material for commercial use in agriculture. The pumice sample shown in Fig. 3 comprises two materials that were differentiated based on the color of the material grains; the sample appears to be mainly composed of white pumice, with a minor amount of black sand, as shown in Fig. 3(a) and Fig. 3(b). This sample was selected after meticulous consideration, including aspects such as the ease of obtaining continuous samples, preserving sample gradation, and striving for more excellent uniformity within the sample. Before conducting further testing on this pumice material, basic testing was first carried out, such as particle size distribution testing, as in Fig. 4. Based on the particle size distribution of the pumice material used, it entered the potential liquefaction zone. Then, physical properties testing was conducted, including particle size distribution (JGS 0131-2009), density of soil particles (ρ_s) (JGS 0111-2009), and minimum–maximum density and void ratio (JGS 0162-2009), as summarized in Table 1. During the basic properties testing, particle breakage was not considered, so the procedure was adjusted to follow standard sand testing methods.

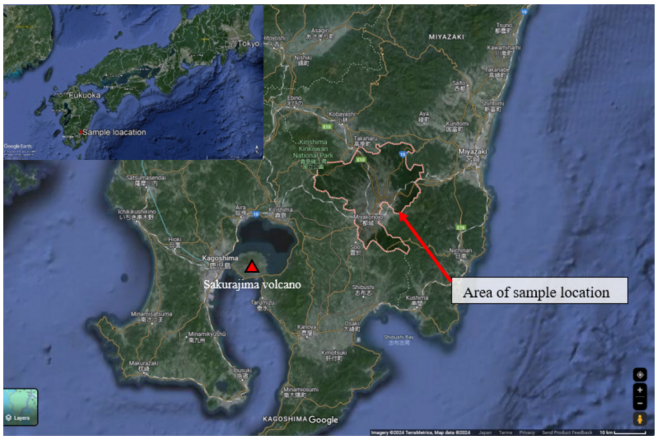

Fig. 2. Sample location.

3. Methodology

3.1. Chemical and microstructural components

First and foremost, the pumice sample is subjected to a drying procedure. Following this, a sequence of fundamental physical tests is carried out, including gradation analysis, density of soil particles (ρ_s) measurement, and relative density evaluation. Before performing further testing, the pumice sample was examined by microscopic inspection using a Scanning Electron Microscope (SEM) to determine the existence of pores inside the pumice. In addition, the chemical components of the sample were determined using X-ray fluorescence (XRF) and Energy-Dispersive X-ray Spectroscopy (EDS). And finally, X-ray diffraction (XRD) testing was carried out to determine the mineral composition of the pumice material being tested.

3.2. Single particle strength test

The particle size distribution test in Fig. 4 reveals that 96.17% of the pumice was retained on the 2.000 mm sieve, 29.71% retained on the 0.850 mm sieve, and 10.07% retained on the 0.425 mm sieve. Subsequently, three particle size groups were categorized as the large (L) sample (retained at 2.000 mm), medium (M) sample (retained at 0.850 mm), and small (S) sample (retained at 0.425 mm) with a total of 135 particles were tested shown in Table 2. A single particle test was carried out using a compression test, with a compression speed of 0.50 mm/min. The orientation of the pumice particles was not strictly controlled as they were placed freely and allowed to reach a stable state before testing. Therefore, the limitation regarding particle orientation in this study was not further examined. The cross-sectional area was calculated through direct measurement using a vernier caliper and the photogrammetry technique.

3.3. One-dimensional consolidation compression test

A one-dimensional consolidation compression test using constant rate strain loading examines soil specimens subjected to continuous loading under one-sided drainage conditions (JIS A 1227: 2009, 2009). The test measures the pressure exerted in the axial direction and the pore water pressure on the undrained surface of the specimen. This test method is employed to characterize the compressibility of pumice. In comparison to traditional one-dimensional consolidation compression tests with continuous step loadings, the test approach offers various advantages: (1) The technique facilitates shorter test durations; (2) It permits the acquisition of continuous data; (3) It enables the autonomous measurement of soil compressibility and permeabil-

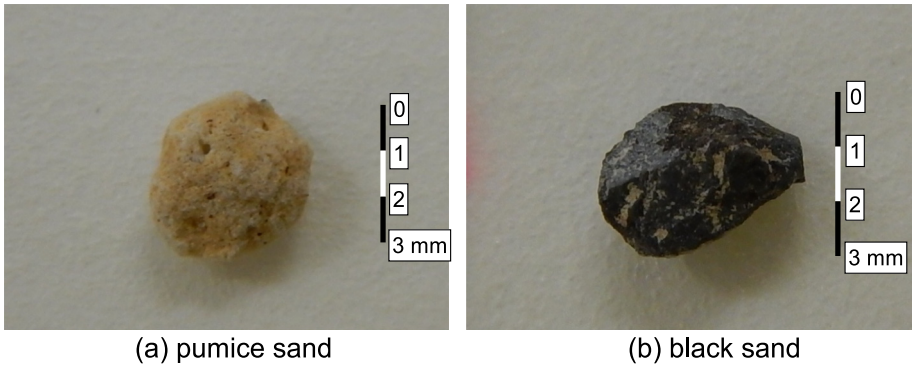

Fig. 3. Pumice sample.

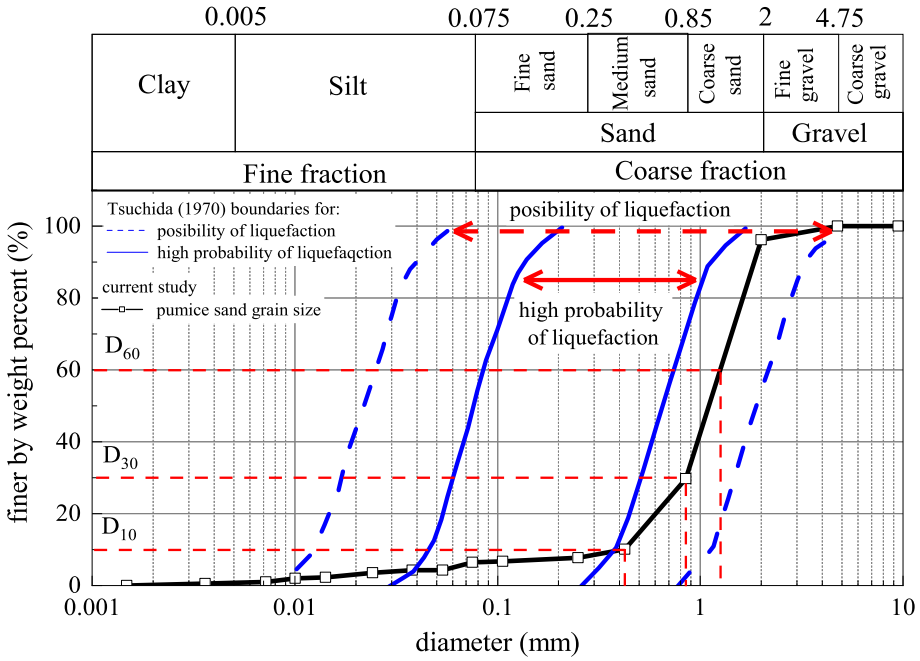

Fig. 4. Particle size distribution.

Table 1
Physical properties of pumice.

Physical properties	
Minimum density (g/cm^3)	0.804
Maximum density (g/cm^3)	0.953
Maximum void ratio	2.156
Minimum void ratio	1.661
Density of soil particles (ρ_s)	2.537

Table 2
Number of samples for single particle strength test.

Sample name	Retained sieve size (mm)	Total test number of
L sample	2.000	45
M sample	0.850	45
S sample	0.425	45

ity without relying on the stress–strain correlation of the soil matrix; (4) It has a broad spectrum of uses, spanning from ultra-soft clay to stiff clay and from organic soil to sandy clay. (5) Automating the testing procedure is straightforward; (6) It does not entail any external disturbance during loading. Therefore, this test method has been used as a condensed approach to decrease testing length. In certain circumstances, however, using a constant strain rate loading approach is imperative, especially when subjecting ultra-soft clay to loads without inducing any distortion or when routinely achieving consolidation characteristics that closely approximate the consolidation yield stress of hard clay.

The compressibility of the pumice was evaluated using a compressibility test following the methodology outlined in the (JIS A 1227: 2009, 2009) standard. Nakata et al. (2001) proposed Eq. (1) to establish the correlation between the tensile strength of single particles and the one-

dimensional consolidation compression test conducted under constant strain loading conditions.

$$F_{sp} = \sigma\left(\sqrt[3]{\frac{(1+e)\pi}{6}}\right)^2 \bar{d}^2 \quad (1)$$

where F_{sp} is the force on a single particle embedded in a soil matrix, σ is the normal stress which refers to yield stress (p_c) in this study, $\bar{d}$ is the mean particle diameter, e is the void ratio.

3.4. Triaxial test

Furthermore, the cyclic triaxial test was performed following the guidelines of JGS 0523-2020 (2020) for the static undrained test, JGS 0524-2020 (2020) for the static drained test, and JGS 0541 for the cyclic undrained test. The samples were created based on the variation of the D_r under two conditions: medium and dense. The triaxial equipment has been correctly configured and the saturation process has been started for each valve. The sample was fabricated according to the guidelines of JGS 0530-2020 (2020) for the preparation of coarse granular material specimens for the triaxial test. Specimens were prepared using the negative pressure technique, and the sample was reshaped by compaction by separating it into multiple layers and compacting it to the specified density by agitation with a hammer. Next, the sample is subjected to a negative suction pressure of −20 kPa in order to maintain its shape once the mold is removed. Within the chamber, the load cell is strategically placed to minimize the impact of friction between the sample and the load cell induced by the connection rod. The triaxial tests were conducted in a controlled laboratory room. The ambient temperature was maintained at 20°C ± 2°C to minimize thermally induced volume changes in the cell fluid and to prevent false pore-water pressure readings. Additionally, the relative humidity of the testing room was kept stable at 65% ± 5%.

In the saturation process, the double negative pressure technique is employed, whereby a negative pressure of −80 kPa is imposed inside the sample, while a negative pressure of −60 kPa is applied externally. This guarantees the maintenance of a constant negative pressure difference of −20 kPa. The water flushing procedure is iterated several times on the sample to remove any entrapped air. This procedure is iterated until the sample completely purges any air. In order to enhance saturation, the sample was subsequently exposed to a back pressure of 200 kPa, as determined by the Skempton pore pressure value ratio (B) being more than 0.95. The sample was allowed to rest for a minimum of 2 h until partial saturation was achieved. Once the necessary Skempton value is achieved, the consolidation process is advanced, and the sample is prepared for static and cyclic testing. Undrained and drained static triaxial tests were conducted at three different confining pressures: 25 kPa, 50 kPa, and 100 kPa, while maintaining a D_r of 60%. Variations of testing conditions for the static and cyclic triaxial test are shown in Tables 3 and 4.

A distinct limitation of the present study is that the experimental program was conducted strictly under constant ambient conditions without evaluating the effects of temperature variations, even though prior literature has demonstrated that different temperature levels can influence mineralogical phase transformations and the resulting hydration compounds (Khayat et al., 2024; Nasiri et al., 2025).

4. Results and discussion

4.1. Geological, chemical, and microstructural characteristics of pumice

According to the 1:200,000 scale geological map of the Miyazaki region, the urban area of Miyakonojo is characterized by extensive distributions of pumiceous materials. As illustrated by the pale yellow zones in Fig. 5, the area comprises widespread deposits of pumice, ash, sand, and gravelly soil; this site served as the exact sampling location for the subsequent analytical and mechanical testing. Stratigraphically, the target deposit is classified as an Ito-type pyroclastic flow underlying the Osumi pumice fall, which originated during the Late Pleistocene epoch of the Quaternary period. Additionally, the geological map delineates several faults and thrusts within the immediate vicinity of the sampling site.

Fig. 6 shows the pumice results from the scanning electron microscope (SEM). It shows that pumice exhibits a consistent distribution of pores throughout its structure, which is believed to contribute to its crushability. Fig. 7 shows the SEM image of black sand, revealing the absence of pores in the material. Given the limited quantity of black sand in the sample, it is reasonable to infer that the overall samples reflect the properties of pumice.

X-ray fluorescence (XRF) study indicates that pumice is composed of 56.5% silica (Si), 16.8% alumina (Al), and 11.2% iron (Fe). Furthermore, Fig. 8 illustrates the presence of lower amounts of additional components, including Calcium (Ca) and potassium (K), together with several other chemical constituents.

EDS analysis is employed in conjunction with SEM testing to investigate the chemical constituents of pumice fur-

Table 3
Testing condition for undrained static triaxial test.

Specimen	Confining (kPa)	Testing conditiom	D_r (%)	B
1	25	Undrained	60.02	97.51
2	50		60.20	95.44
3	100		60.45	96.78
4	25	Drained	61.05	96.55
5	50		60.81	96.08
6	100		60.35	96.49

Table 4
Testing condition for undrained cyclic triaxial test.

Specimen	Confining (kPa)	D_r (%)	B
1	50	43.24	98.38
2		41.36	96.23
3		40.89	98.56
4		42.37	98.04
5		73.89	97.56
6		71.10	98.38
7	100	40.99	96.23
8		44.37	96.06
9		40.90	96.89
10		42.38	96.09
11		70.13	96.30
12		71.34	97.06
13		71.47	97.40
14		74.57	96.35

ther, this is the strategic selection of particular chemical constituents on the surfaces of materials for investigation. Fig. 9(a) shows the observation sites of the EDS data on the surface of the white pumice. Fig. 9(b) shows the location of the EDS data observation sites for the black sand. The outcome of the EDS analysis is depicted in Fig. 10. Fig. 10(a) illustrates a comparison of the chemical constituents of white pumice. The analysis indicates that oxygen (O) is the main chemical component, accounting for 61.3% of the mass. Silicon (Si) accounts for 21.7% of the composition, while aluminum (Al) makes for 7.4%. Furthermore, lesser quantities of other minerals, such as calcium (Ca) and iron (Fe), are also found. A summary of the chemical constituents of black sand is presented in Fig. 10(b). The EDS analysis shows that oxygen (O) is

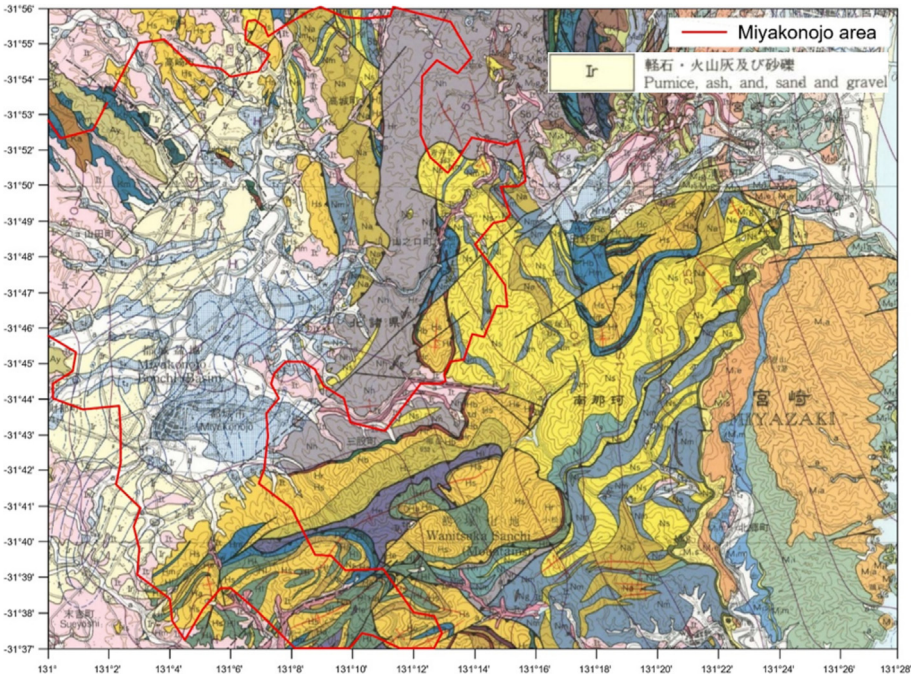

Fig. 5. Geology condition of Miyakonojo area (modified from Saito et al. (1997)).

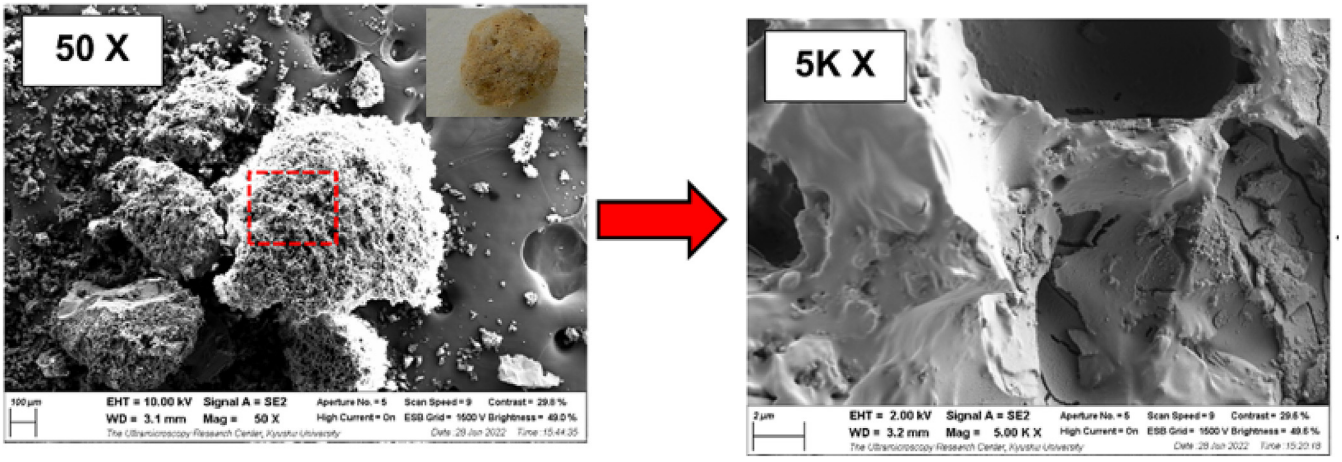

Fig. 6. SEM results of pumice sand.

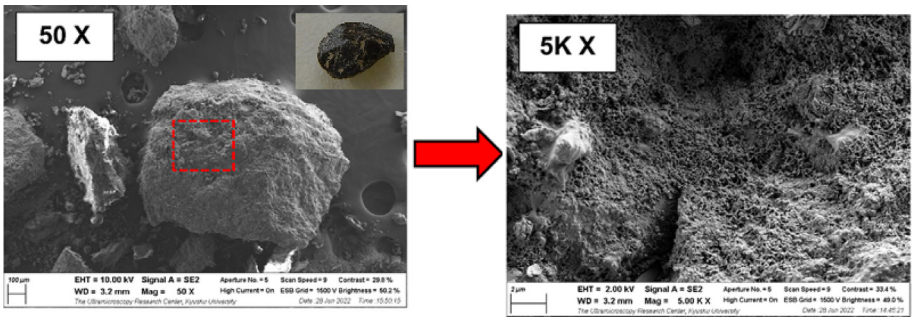

Fig. 7. SEM results of black sand.

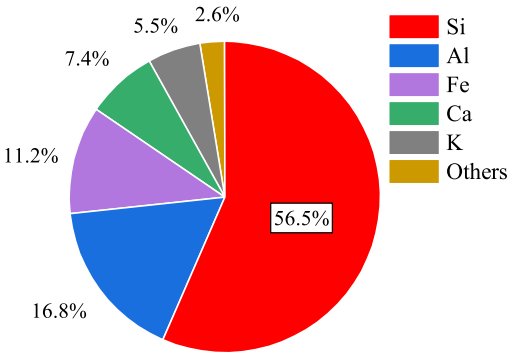

Fig. 8. Chemical component of pumice sample based on XRF.

the main chemical component in black sand, present at 72.7%, followed by silica (Si) at 6.4% and aluminum (Al) at 9.9%. Other minerals, such as manganese (Mn) and iron (Fe), are also observed. The chemical component is consistent with the findings of previous studies, which confirmed that pumice is predominantly composed of silica (SiO_2) and alumina (Al_2O_3) crystals (Kobayashi et al., 1991; Mboya et al., 2011). Consistent with findings from recent literature, other researchers have also demonstrated a similar chemical profile, confirming that silica is the primary component of pumice. For instance, XRF analysis conducted by Nasiri et al. (20244) revealed that the material is pre-

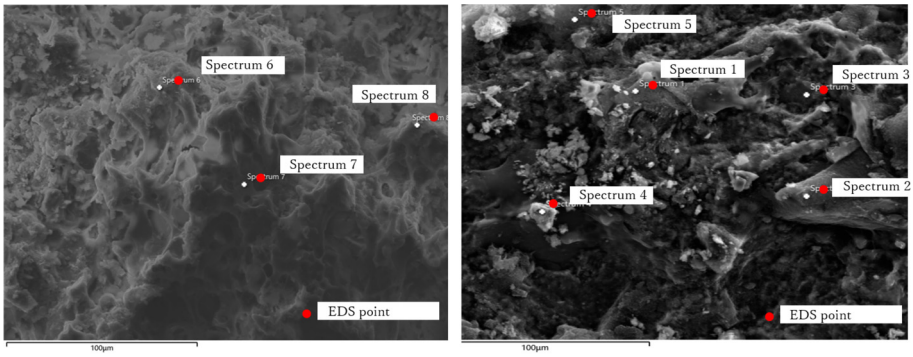

Fig. 9. Sampling point for EDS testing (Basoka et al., 2024a).

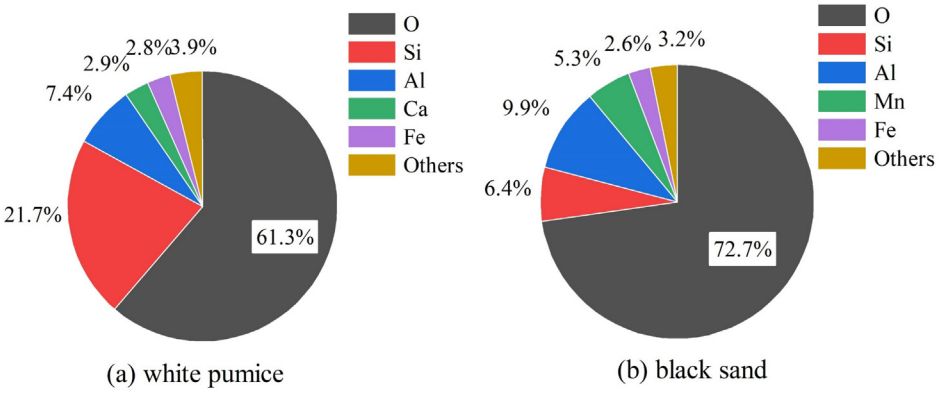

Fig. 10. Chemical results from EDS (Basoka et al., 2024a).

dominantly composed of silicon and aluminum—together accounting for approximately 79% of its total mass—with active silica (SiO_2) specifically making up around 64% of the composition.

XRD test was conducted to determine the mineral constituents of the pumice. Analysis of the mineral components of the pumice was conducted using the PXDL2 software, and the findings are presented in Table 5. A preliminary reference for selecting the candidate mineral and chemical component for pumice is derived from the results of XRF and EDS tests. Mineral component quantification can be achieved using the whole powder pattern fitting (WPPF) technique. Analysis of XRD indicates that the main mineral constituents in pumice are quartz (SiO_2), accounting for 66.7% (with a figure of merit of 0.914) and cristobalite-alpha (SiO_2) for 33.3% (with a figure of merit of 1.482). Although they have different crystalline forms, both minerals contain the same chemical constituent SiO_2 (Gibson and Lafemina, 1996; Tang et al., 2015). From a comparison with the mineral composition of typical Toyoura sand, it is evident that the primary minerals found in Toyoura sand are 75% quartz, 22% feldspar, and 3% magnetite (Oda et al., 1978). The mineral constituents of pumice and Toyoura sand are similar in that quartz is the predominant mineral component.

4.2. Single-particle strength

Typical test results from the single-particle strength test, as shown in Fig. 11, exhibit a distinctive jigsaw-like pattern. The first deflection observed in the load–displacement curve is regarded as the strength of the particle, representing the point of initial cracking or the onset of failure. Subsequent peaks occur as the fractured material undergoes rearrangement, temporarily increasing its strength before reaching final failure. Consistent with previous studies on single-particle strength, this research defines particle strength based on the first failure event to ensure comparability with earlier findings. Each pumice particle was carefully placed on a flat surface and allowed to stabilize prior to testing. The cross-sectional area of each particle was determined through direct measurement using a vernier caliper and further verified using the photogrammetry technique. When analyzing the test results of pumice particles in this study, as shown in Fig. 12, it is evident that the single-particle strength of pumice is lower compared to other granular materials such as carbonate sand and Toyoura sand.

Fig. 13 illustrates the relationship between single-particle strength and particle diameter, demonstrating that

Table 5
Mineral component of pumice material.

Mineral name	Formula	Figure of merit	Content (%)
Quartz	SiO_2	0.914	66.70
Cristobalite-alpha	SiO_2	1.482	33.30

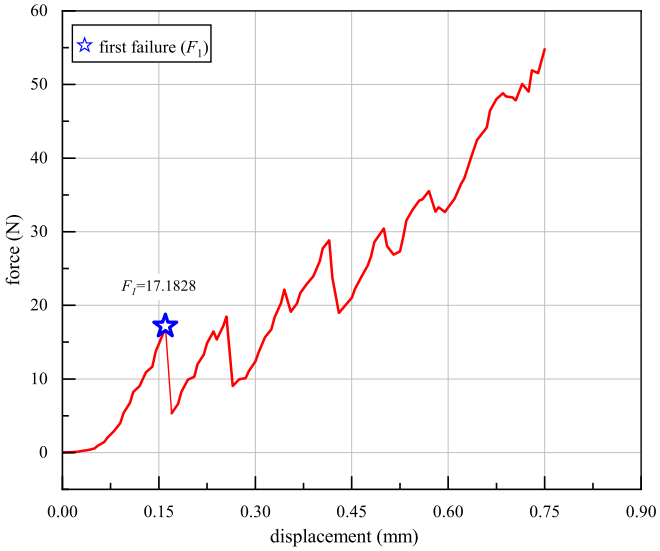

Fig. 11. The typical test result of single-particle strength.

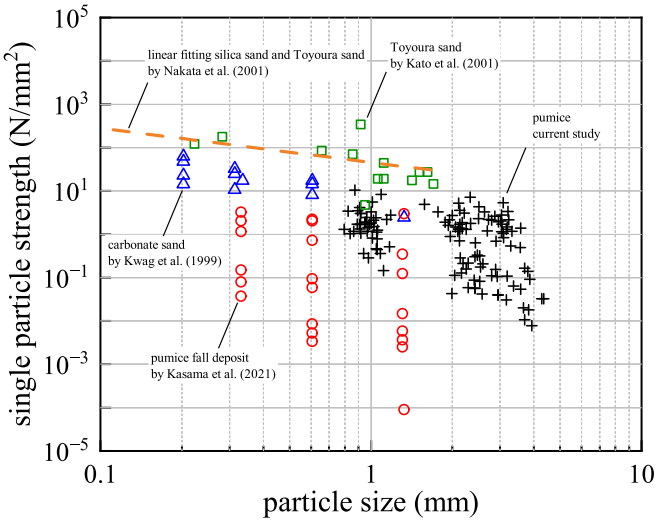

Fig. 12. Comparison of single-particle strength results.

single-particle strength rises as the pumice diameter size decreases. The red line in Fig. 13 has been determined as the regression line between the single-particle strength and particle diameter using the dataset of 135 data points. A fitting line is employed to ascertain the mean size of each particle group. The mean size is projected onto the fitting line to derive a representative strength of individual particles for each group, as illustrated in Table 6. The size difference between M and S particles is due to the inherent non-uniformity of particle sizes within the sample. However, despite this variation, the size difference between M and S does not significantly affect the testing results, as the regression line for particle strength considers the entire dataset, including S, M, and L sizes.

To analyze the impact of particle shape, namely the aspect ratio and roundness coefficient illustrated in Fig. 14 and calculated using Eqs. (2) and (3), on the out-

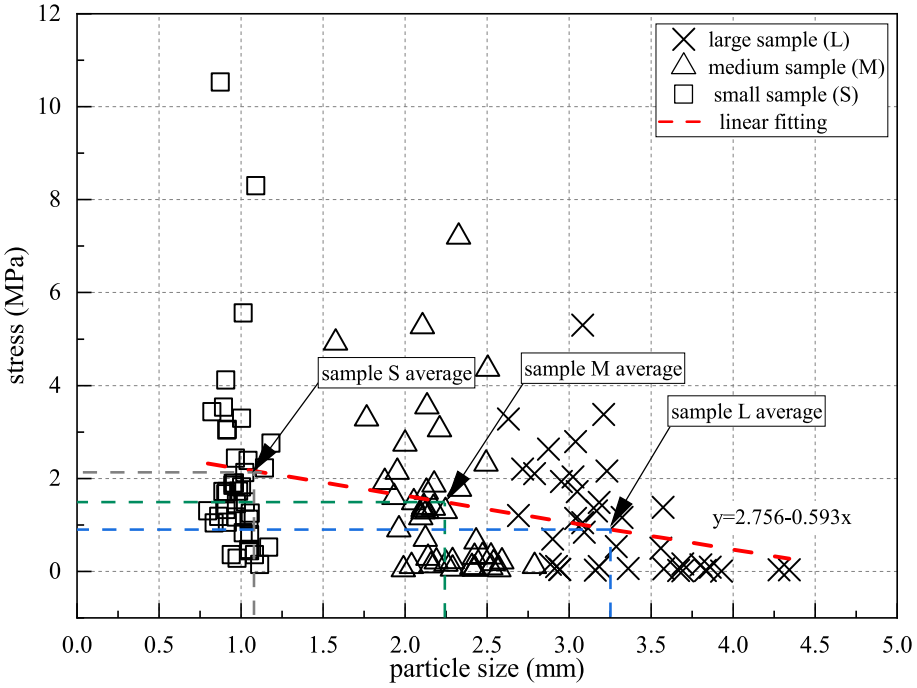

Fig. 13. Overall single-particle strength test results.

Table 6
Average size and single-particle strength based on single-particle strength test.

Sample	Particle size	Stress	Force
	(mm)	(MPa)	(N)
L	3.25	0.8282	28.4547
M	2.22	1.4367	15.8202
S	1.14	2.0814	3.06377

comes of the single-particle strength test, Fig. 15 illustrates the correlations between single-particle strength, aspect ratio, and roundness coefficient. According to Fig. 15(a), the association between aspect ratio and single-particle strength is insignificant and lacks a distinct relationship between the two parameters. Fig. 15(b) demonstrated a negligible association between particle roundness and single-particle strength. The link between aspect ratio and roundness is seen in Fig. 16. It illustrates that the magnitude of the roundness coefficient rises as the aspect ratio increases.

$$aspectratio = \frac{majoraxis}{minoraxis} \tag{2}$$

$$roundnesscoefficient = \frac{(particleperimeter)^2}{4\pi A} \tag{3}$$

4.3. One-dimensional consolidation compression

Fig. 17 illustrates the outcomes of the one-dimensional consolidation compression test conducted on pumice under constant strain loading conditions. These results are compared to similar tests conducted on clay by Mesri and Feng, (2019) and Toyoura sand by Nakata et al. (2001).

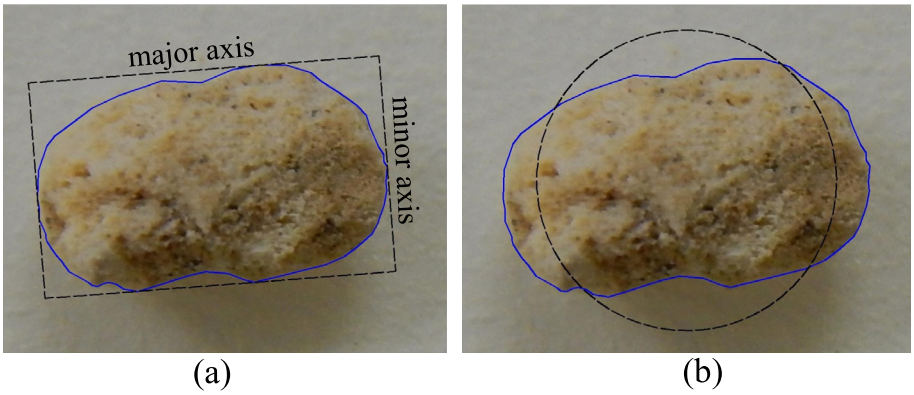

Fig. 14. Particle shape (a) aspect ratio (b) roundness (Basoka et al., 2024b).

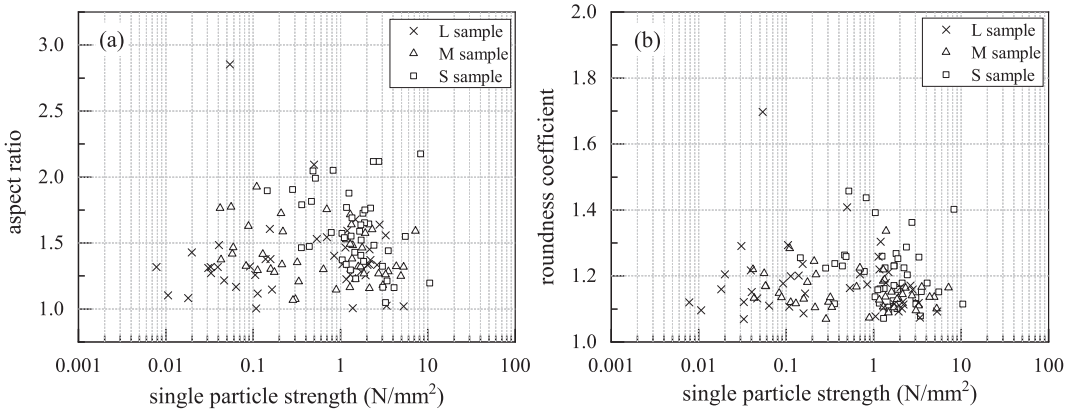

Fig. 15. The relationship between particle strength, aspect ratio, and roundness coefficient (Basoka et al., 2024b).

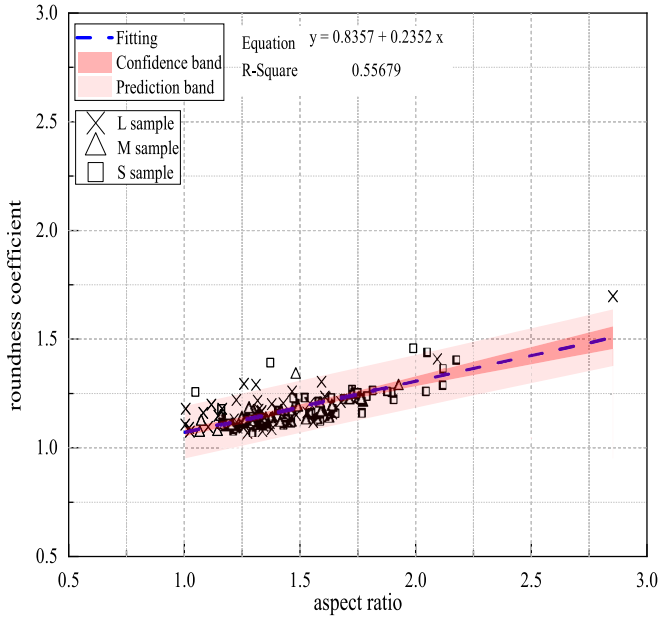

Fig. 16. The relationship between aspect ratio and roundness coefficient.

The yield stress (p_c) in this consolidation test conducted in one dimension, with a constant rate of strain loading, can be regarded as the factor that triggers the crushable behavior of the pumice particle. The p_c of pumice is positioned between clay and Toyoura sand, although pumice may appear the same as sand, its pore structure results in a lower p_c than Toyoura sand and a larger p_c than clay.

Furthermore, a comparison of the results obtained from the study conducted by Kasama et al. (2006) on the p_c of different materials indicates that the present investigation of pumice demonstrates a lower p_c position compared to the other materials, as visualized in Fig. 18. The test results suggest that pumice is more likely to be crushed since a lower p_c is associated with higher crushability. Moreover, the relationship between the D_r and p_c of pumice is similar to that of other materials, where an increase in D_r results in an increase in the p_c. Concerning Fig. 17, we can derive the p_c and compression index (C_c) for each D_r value of pumice, as shown in Table 7.

Fig. 19 shows the relationship between the strength of individual particles in a single particle strength test and a one-dimensional consolidation compression test while maintaining a consistently applied strain loading rate. According to Eq. (1), the p_c is transformed into F_{sp} for the pumice. The results indicate a strong correlation between the single-particle strength of pumice and increasingly higher D_r values.

4.4. Static undrained triaxial test

4.4.1. Strength parameter

The diagram in Fig. 20 shows Morh's circle and presents the shear strength parameter for undrained and drained states. Under undrained conditions, the cohesion is 25.93 kN/m^2, and the friction angle is 51.07°. Under drained conditions, the cohesion value is measured to be 11.99 kN/m^2, while the friction angle is obtained at 35.85°. The results of each sample from these static tests also demonstrate that the confining pressure directly influences the mechanical properties of the pumice, exhibiting a structural behavior similar to that of conventional sand. This observed phenomenon aligns with previous investigations conducted on sandy materials by Khayat (2018); Umar et al. (2019); Vranna et al. (2021).

4.4.2. Stress path

The stress path under undrained and drained regimes is shown in Fig. 21, several studies also elucidated the stress path under undrained and drained conditions using selected representative lines (Ishihara et al., 1975; Kang et al., 2019; Umar et al., 2019). This picture displays the steady-state line corresponding to undrained conditions and the critical-state line indicative of drained situations. The steady-state line appears in an elevated position relative to the critical-state line. Nevertheless, the disparity between the steady-state line and the critical-state line is negligible. This convergence can be specifically ascribed to the high compressibility and pronounced grain crushability of the pumice material. Under progressive shearing, extensive particle breakage alters the grain size distribution

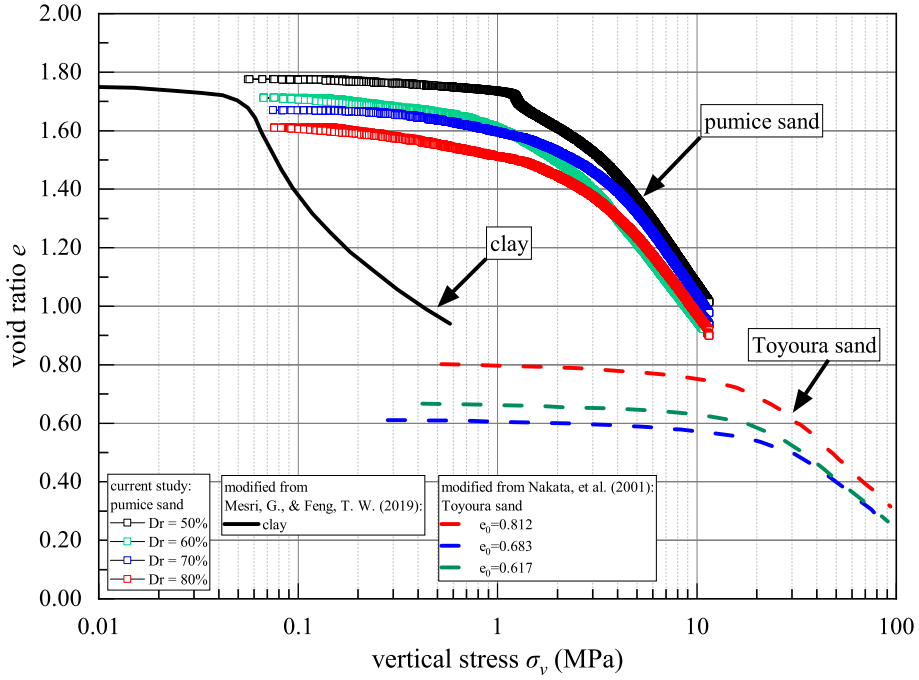

Fig. 17. Constant strain rate consolidation test result (Basoka et al., 2024).

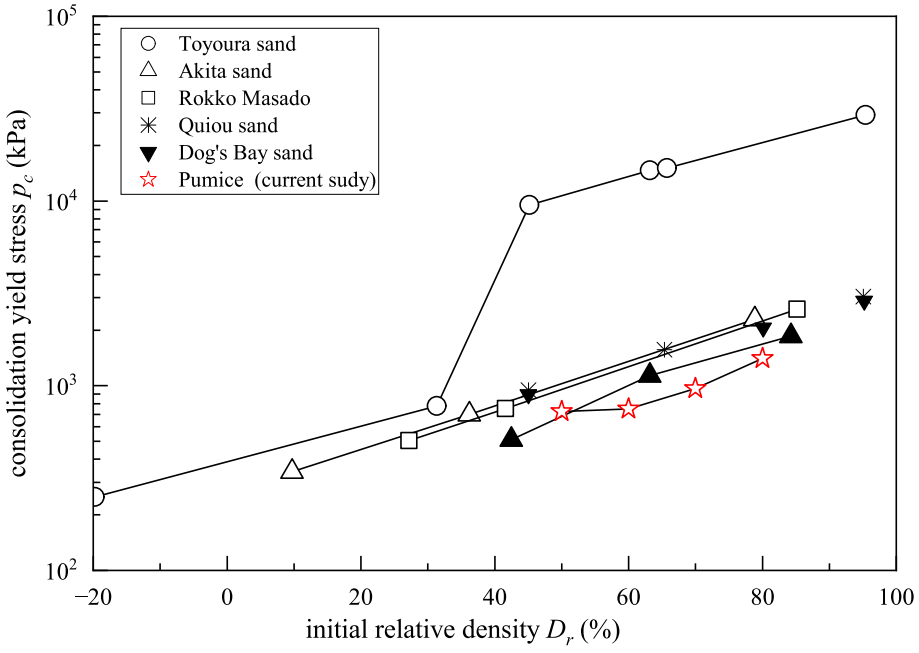

Fig. 18. Yield stress comparison (modified from Kasama et al. (2006)).

Table 7
Yield stress and compression index of pumice.

Relative density D_r (%)	Yield stress p_c (MPa)	Compression index C_c
50	0.724	0.810
60	0.749	0.936
70	0.965	0.569
80	1.048	0.640

and effectively erases the memory of the initial structural fabric. This dominant crushing mechanism suppresses fabric-dependent structural variations, forcing the volumetric and effective stress states at both the steady and critical states to collapse onto a single, unique ultimate state line. It is also possible to detect the flow liquefaction line, which indicates the rate at which the mean effective stress

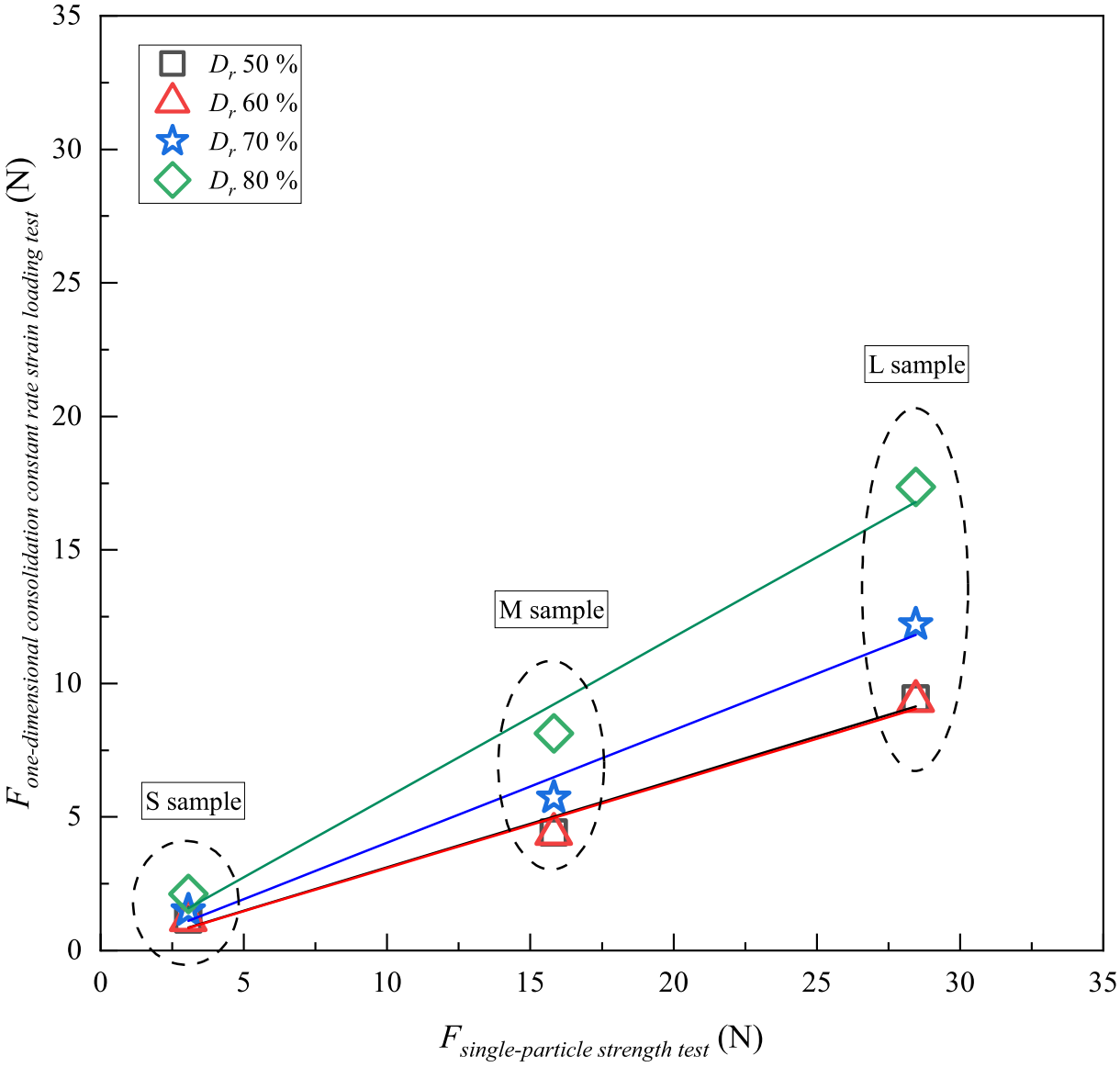

Fig. 19. Correlation of single-particle strength of one-dimensional consolidation compression constant rate strain loading test and single-particle strength test.

changes during the contractive phase. This line indicates the point at which liquefaction begins.

Furthermore, the phase transition line can be determined, which represents the lowest average practical stress value of each stress pathway when the system is drained. This line symbolizes the shift from contraction to expansion. As previously explained, analyzing these line boundaries represents the liquefaction response to static loads.

4.5. Cyclic undrained triaxial test

Fig. 23 shows the relationship between the *CSR* and the number of cycles for specimens 1–14. The data presented in Fig. 23 illustrate that an increased *CSR* results in a reduced number of cycles required to cause liquefaction (double amplitude (*DA*) 5% or pore water pressure ratio (r_u) > 0.95). Fig. 24 illustrates the gradual rise in pore water pressure as the number of cycles increases, the large variation in porewater pressure during a cycle of loading in cyclic triaxial tests occurs because the soil undergoes alternating phases of compression and expansion. When the soil contracts, porewater pressure increases, and when it dilates, porewater pressure decreases. This behavior depends on soil density, loading conditions, and how the soil particles rearrange under cyclic stress. The correlation between deviatoric stress and axial strain under low strain exposes a characteristic in the cyclic response of a material referred to as the shear modulus (*G*) shown in Fig. 22. This work demonstrates the estimation of the shear modulus using Eq. (4), which is coupled to the Young modulus (*E*). The Young's modulus can be determined by using Eq. (5). In the calculation of shear modulus using Eq.

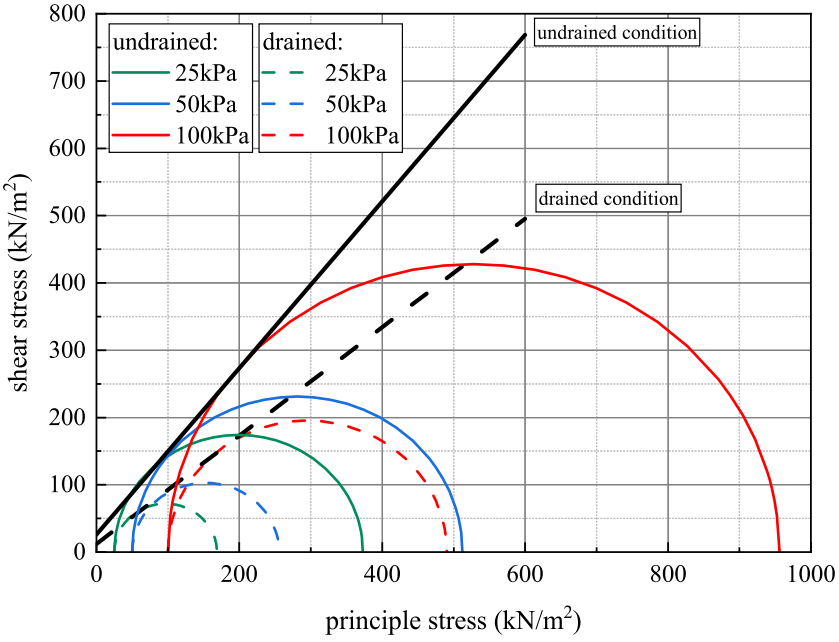

Fig. 20. Mohr circle of undrained and drained conditions.

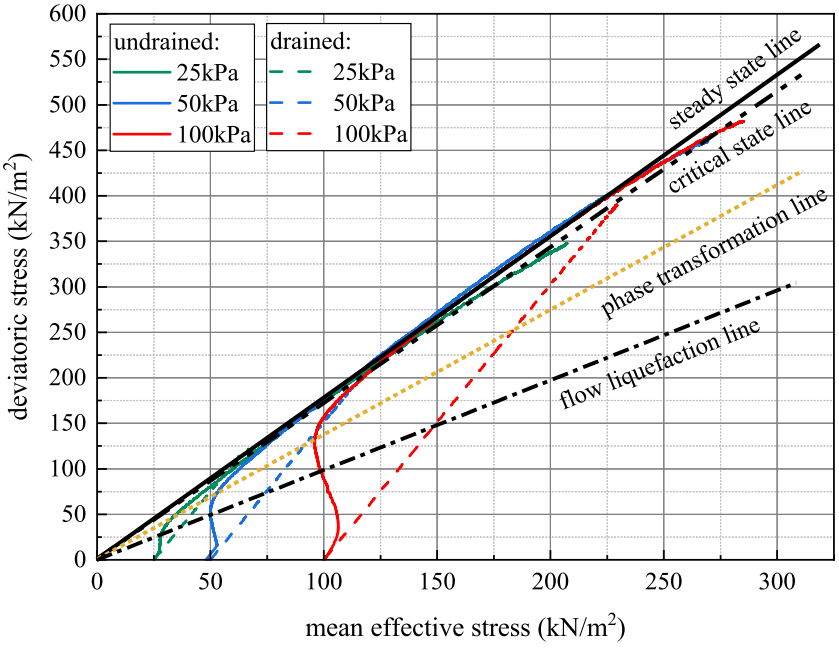

Fig. 21. Stress path under undrained and drained conditions.

(4), it was assumed that the Poisson's ratio (v) is 0.50 under undrained circumstances.

$$G = \frac{E}{2(1+v)} \tag{4}$$

$$E = \frac{2\sigma_c}{(\varepsilon_1 + \varepsilon_2)} \tag{5}$$

As highlighted in recent studies by Chindaprasirt et al. (2022) and Nasiri et al. (2024b), evaluating soil stiffness and elastic modulus provides critical insights into structural behavior. Accordingly, this study examines variations in elastic modulus across different sample treatment conditions to bolster the overall mechanical interpretation. Figs. 25 and 26 illustrate the variations in the elastic properties of the specimens, specifically focusing on the E under varying CSR, σ_c, and D_r. As demonstrated in these figures, a distinct inverse relationship is observed between E and CSR, where higher cyclic load amplitudes induce severe stiffness degradation due to accumulated plastic strains. Conversely, the stiffness exhibits a strong positive correla-

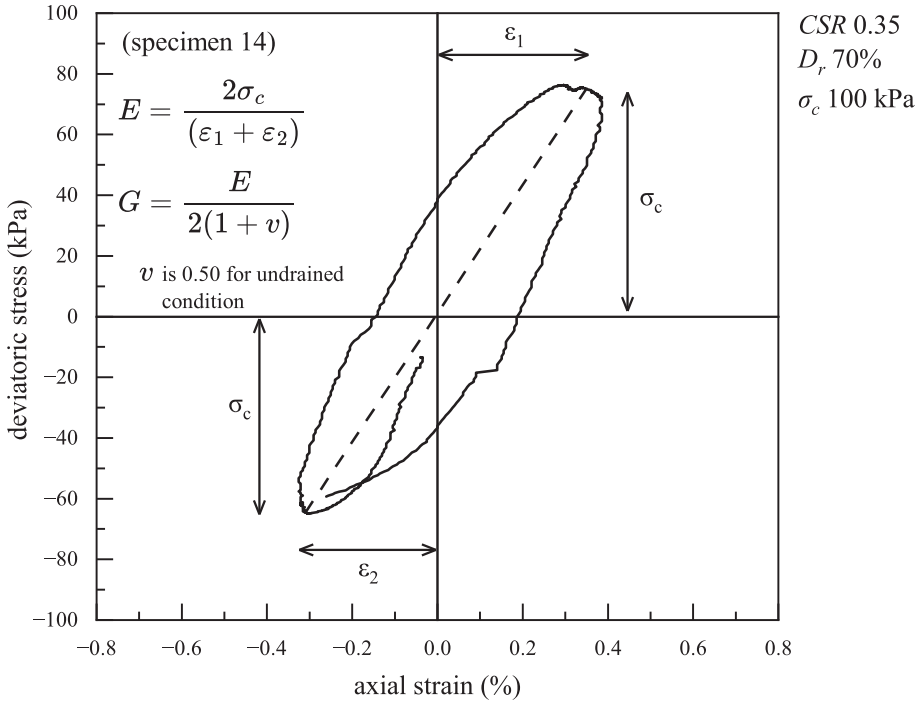

Fig. 22. Typical of deviatoric stress versus axial strain for small strain (1st cycle) to calculate young modulus (example specimen 14).

tion with both the confining pressure and relative density. The increase in σ_c and D_r enhances the inter-particle contact area and effective stress, thereby significantly boosting the material's resistance to cyclic deformation.

The correlation between G with σ_c and D_r is depicted in Fig. 27 under the same σ_c conditions, an incremental rise in D_r results in elevated G values. Fig. 28 demonstrated that when the σ_c is increased, the values of G for the same D_r also increase.

For liquefaction behavior can be seen in Fig. 29, a clear correlation exists between the increase in σ_c and the reduced cycle loadings required to reach the liquefaction condition. A greater σ_c of 100 kPa decreases the resistance to liquefaction, reducing the cyclic loadings needed at a σ_c of 100 kPa and an increased number of cycles needed at a σ_c of 50 kPa, this phenomenon is unlike the typical dynamic response, where the cycle tends to shrink as σ_c increases. The unique porosity of pumice is likely one of the reasons for this behavior. A study by Orense and Pender (2013) also showed similar results. For the variation of D_r, it can be seen that increasing D_r also increases the liquefaction resistance of pumice. A comparison was made between the results of the current study and those of previous research, as shown in Fig. 29. In Fig. 29, (Hyodo et al., 1994) demonstrated that the liquefaction resistance of sand materials is generally unaffected by σ_c. However, Pumice, in particular, shows a distinct dependence of liquefaction resistance on confining pressure, as supported by Orense and Pender (2013) based on the test results for Pumice obtained from New Zealand. Regarding the impact of relative density Dr on the liquefaction resistance, the pumice property is comparable to that of other materials like sand. Asadi et al. (2022) demonstrated that a rise in *Dr* results in a corresponding increase in liquefaction resistance.

Although the morphological analysis in this work was limited to individual particle characteristics rather than a global assembly characterization, the shape and sphericity of the grains remain critical factors. Pumice particles are inherently angular with low sphericity, which promotes strong particle interlocking during triaxial shearing. This morphology restricts particle rotation and increases shear resistance compared to smoother, sub-rounded sand grains (Huang et al., 2023; Zhang et al., 2020). While the collective effect of shape variations could not be directly isolated in this study, the high angularity of the pumice is expected to have a pronounced impact on the overall shear strength and volumetric behavior of the mixture.

4.6. Particle size evolution

4.6.1. Static condition

Through the analysis of the variation in particle size gradation following undrained and drained triaxial compression experiments, as depicted in Fig. 30, it is evident that the particle crushability of pumice is higher under drained conditions. This behavior is strongly correlated with the

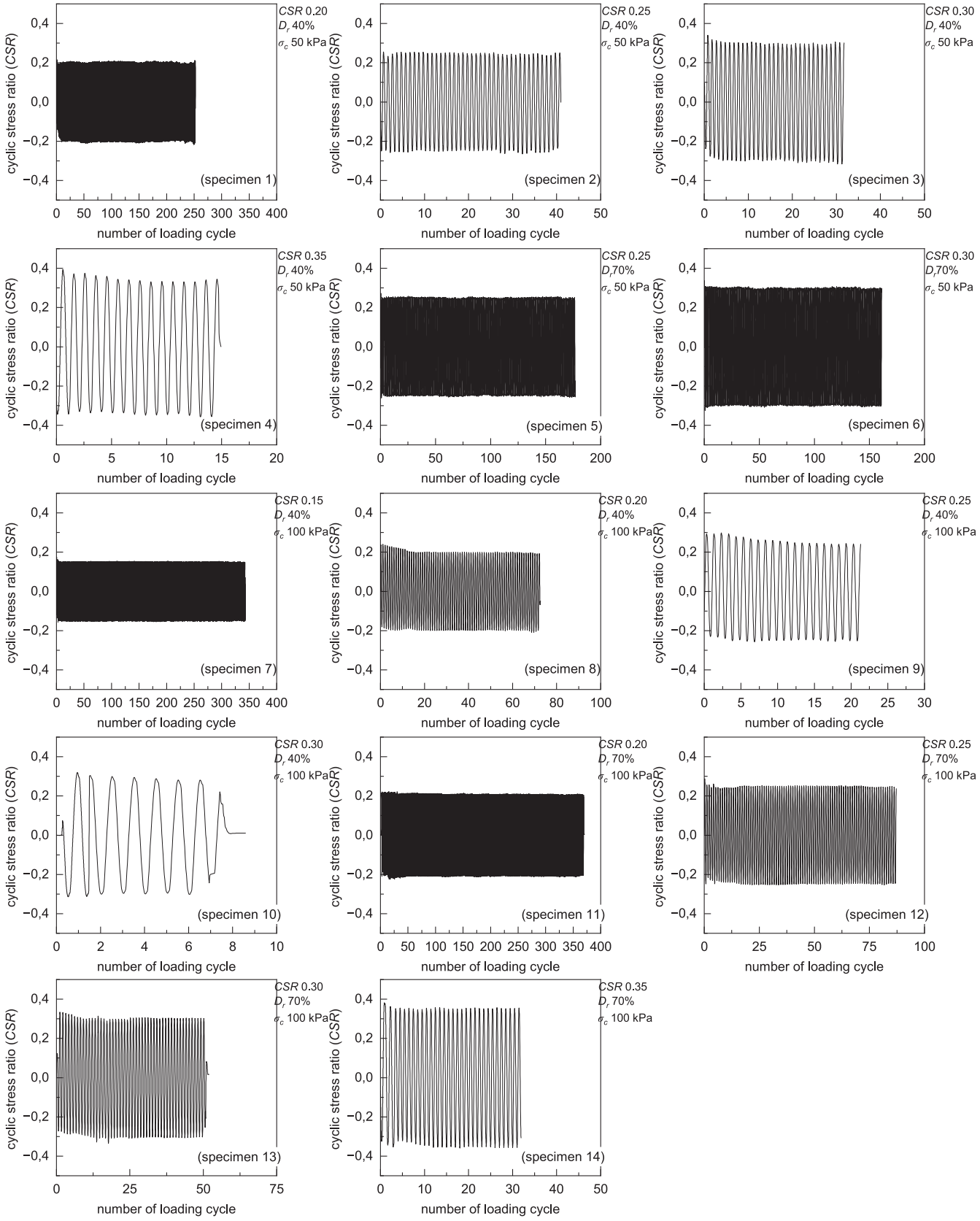

Fig. 23. Cyclic stress ratio versus number of cycle.

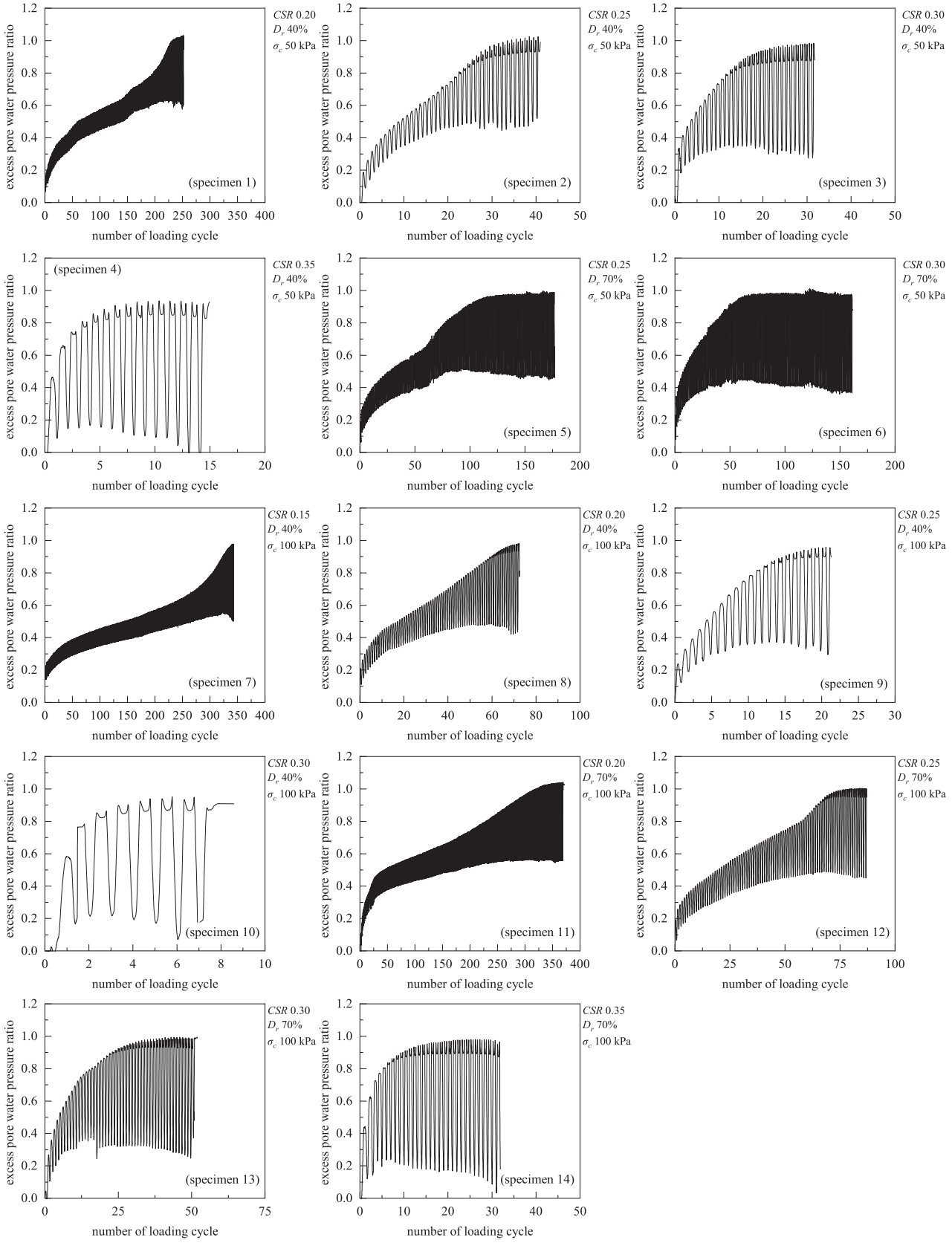

Fig. 24. Excess pore water pressure versus number of cycle.

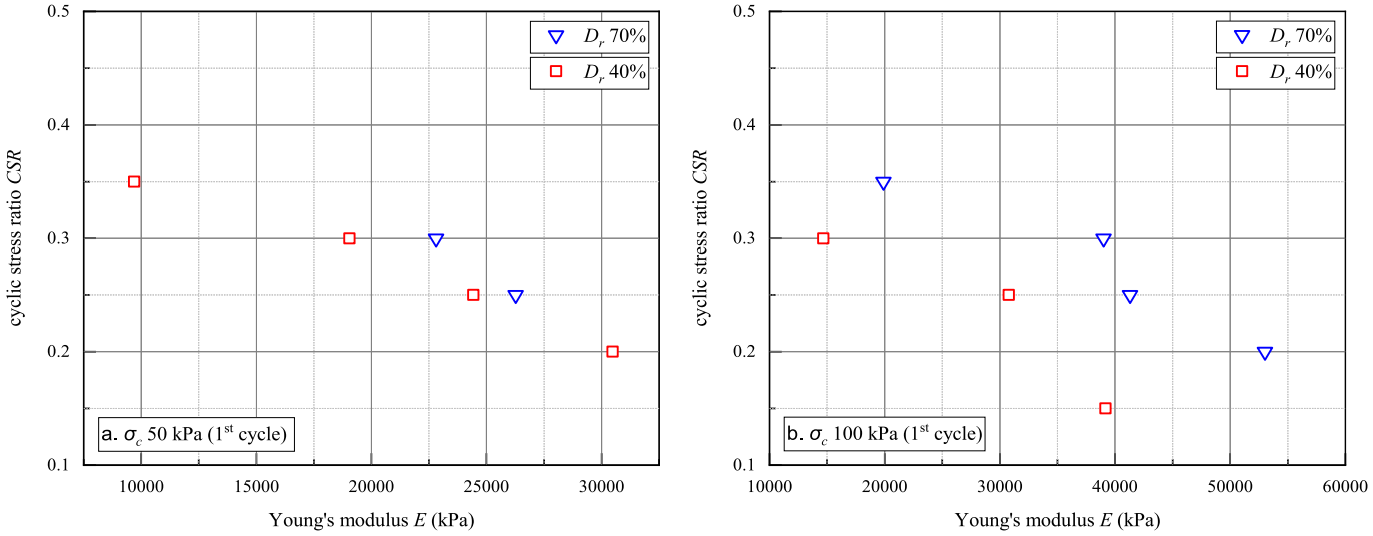

Fig. 25. Young's modulus behavior based on confining pressure.

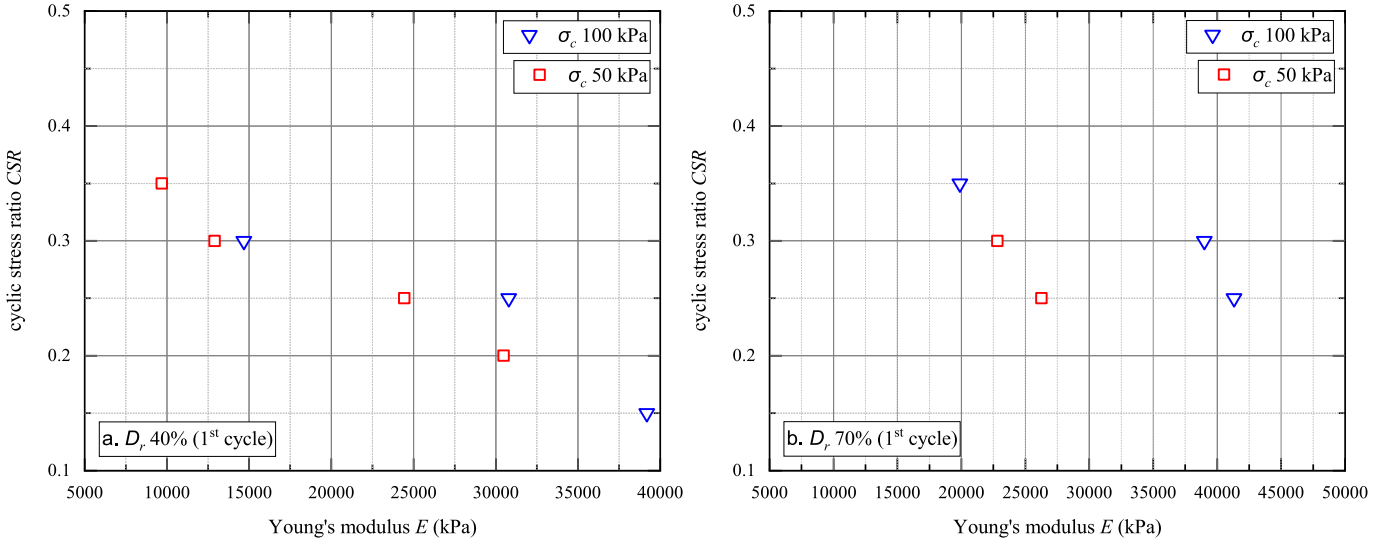

Fig. 26. Young's modulus behavior based on relative density.

compressibility of pumice. The crushable nature of pumice consequently decreases its shear strength under drained circumstances.

4.6.2. Cyclic condition

The degree of particle crushability of pumice caused by cyclic load was evaluated by analyzing the particle size distribution after completing the cyclic undrained triaxial test, as depicted in Fig. 31. The test result pertains to the sample having a *CSR* 0.30. The results of the one-dimensional consolidation compression test indicate that the pumice requires yield stress ranging from 0.72 MPa to 1.05 MPa under relative density conditions from 50% to 80% to achieve particle crushability. Nevertheless, when the *CSR* is 0.30, the highest axial stress recorded is a mere 0.03 MPa, while the confining pressure is much lower at 0.10 MPa. These two stresses have yet to reach the point of minimum yield stress, resulting in negligible alterations in particle size.

In Fig. 31, a magnification section was established at the particle size distribution change, and an analysis of the two positions revealed that the lower D_r displayed higher crushability under the same confining pressure, as seen by the reduction in D_{30} and D_{60} values. Furthermore, when subjected to the same density conditions, the higher confinement results in the formation of finer particles, suggesting an increased crushability level. Although the observed variations in gradation support the conclusions of earlier studies (Fangwei, 2018; Gupta, 2016; Hyodo et al., 2016), further experimentation is necessary to investigate the

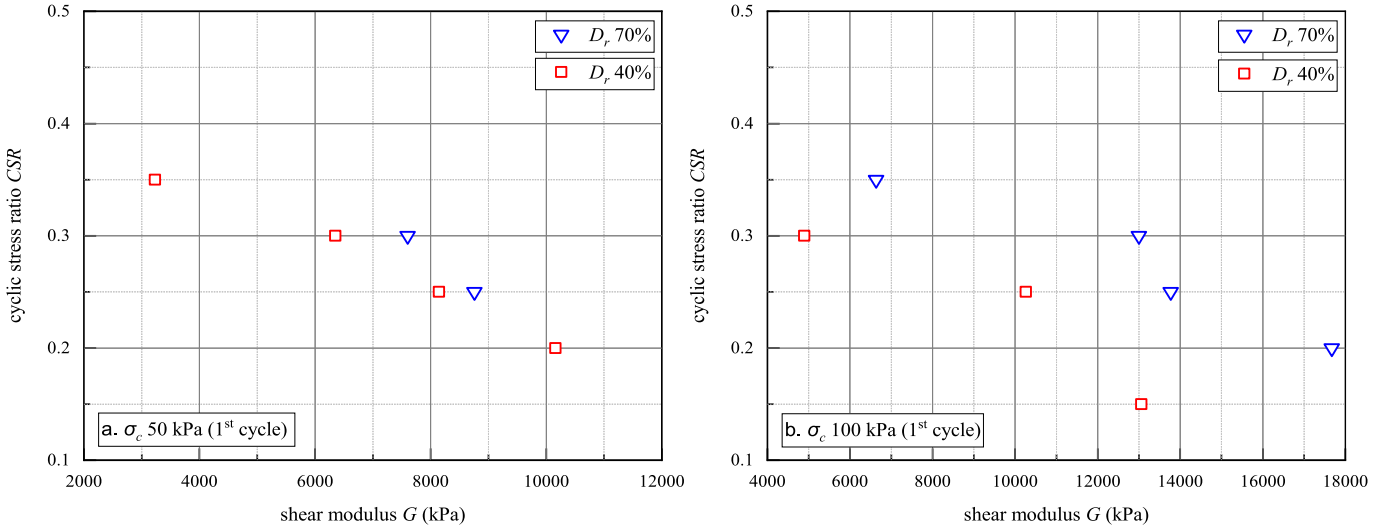

Fig. 27. Shear modulus behavior based on confining pressure.

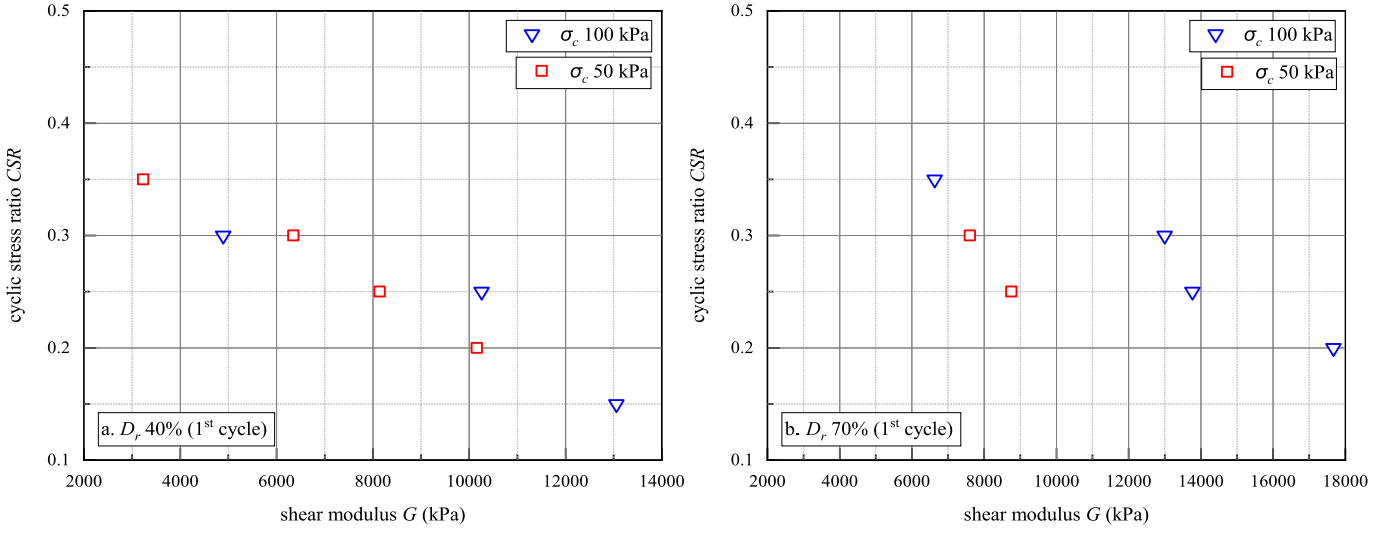

Fig. 28. Shear modulus behavior based on relative density.

response of pumice under high confining pressures above its yield stress in order to gain a more comprehensive knowledge of the impact on crushability.

5. Conclusions

The comprehensive analysis undertaken in this study yields several key conclusions regarding the physical and mechanical behavior of the pumice material from the Miyakonojo region. Material characterization indicates that silica (SiO_2) serves as the predominant chemical component of the pumice. At the micro-scale, single particle strength testing established that the individual particle strength varies between 3.06 N and 28.45 N for average particle diameters ranging from 1.14 mm to 3.25 mm. Furthermore, macro-mechanical evaluation via one-dimensional compression tests reveals that the yield stress of the pumice falls within the range of 0.724 MPa to 1.048 MPa under variations in relative density (D_r) from 50% to 80%, effectively positioning the yield characteristics of this volcanic material between those of standard sand and clay.

Regarding shearing and dynamic behavior, static triaxial tests demonstrate divergent responses depending on the drainage boundaries; the pumice exhibits strain-hardening behavior under undrained conditions, whereas it transitions to strain-softening behavior under drained conditions. This phenomenon is closely tied to the grain crushability, as comparative pre- and post-test sieve analyses quantitatively demonstrate a higher degree of particle breakage and grain degradation under drained shearing. Consequently, drained tests yield a greater abundance of fine particles, leading to a lower overall shear strength in treated conditions compared to undrained states. Finally,

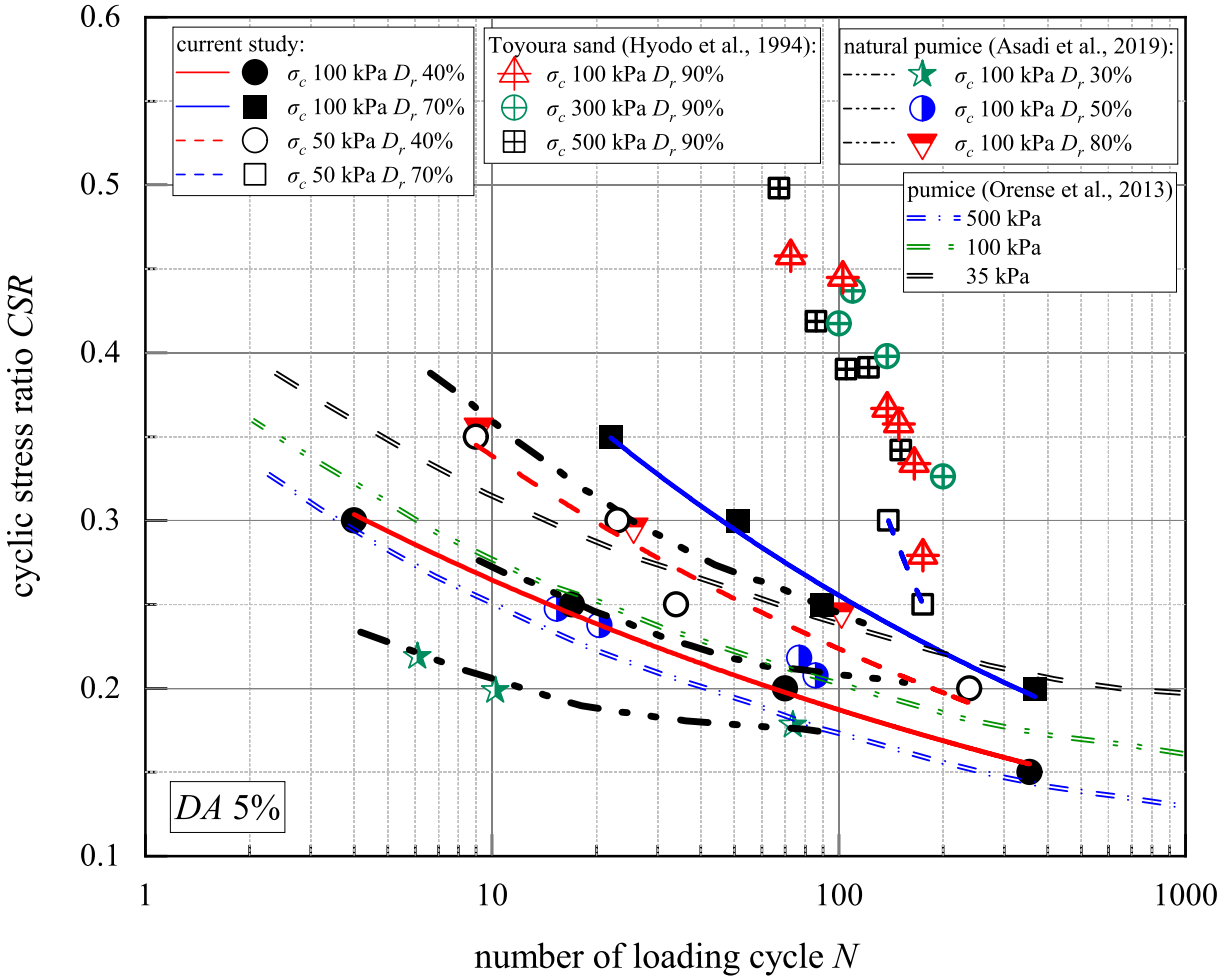

Fig. 29. Comparison of liquefaction resistance with other studies.

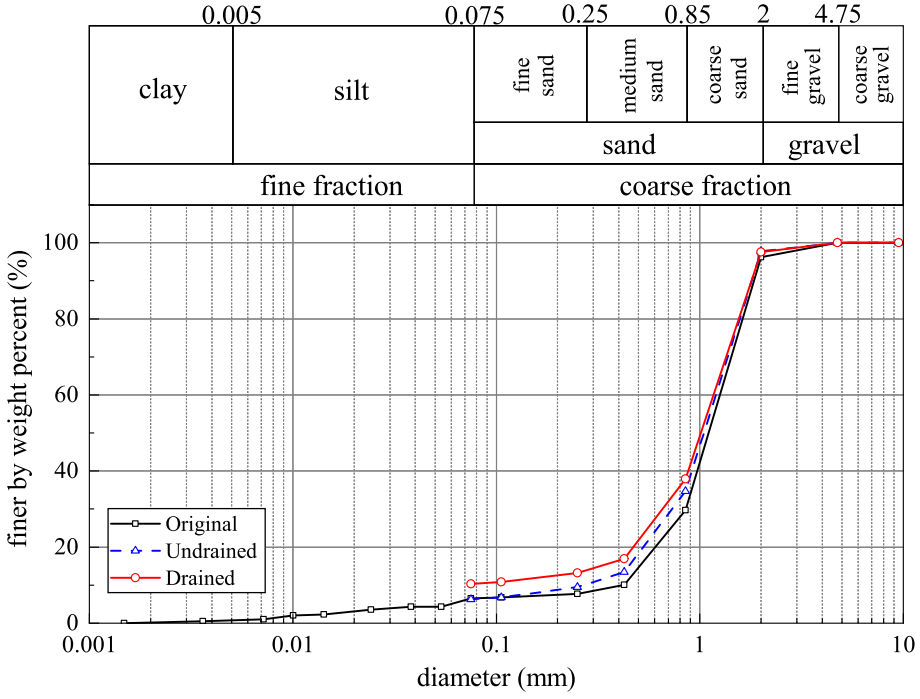

Fig. 30. Particle size distribution before and after static triaxial test.

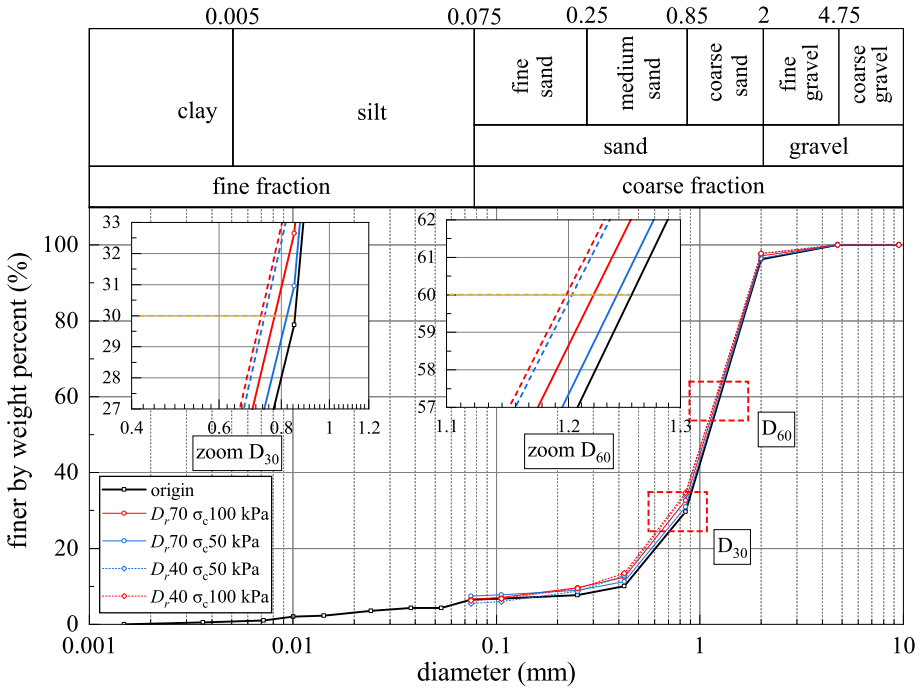

Fig. 31. Particle size evolution after cyclic undrained triaxial test.

cyclic liquefaction analysis reveals a strong dependency between the liquefaction resistance of the pumice and variations in confining pressure, demonstrating that liquefaction resistance diminishes with the augmentation of confining pressure. This highlights the crucial role of selecting appropriate confining pressures in both laboratory testing and engineering design.

While these findings offer valuable insights, it is important to outline the boundaries and limitations of the experimental program presented herein. Firstly, the morphological analysis of the pumice (shape and sphericity) was conducted at a single-particle scale, meaning the collective, assembly-scale impact of grain morphology on the macro-mechanical response was not systematically isolated. Secondly, the engineering parameters derived in this work specifically reflect the characteristics of pumice from the Miyakonojo region under the defined laboratory boundary conditions. Therefore, expanding the geographical scope of sampling is highly recommended for future works to establish a more generalized framework regarding the overall liquefaction resistance behavior. Nonetheless, the internal mechanisms of the mixture, particularly regarding grain degradation, were rigorously quantified using the aforementioned pre- and post-test sieve analyses, thereby ensuring the validity and reliability of the reported stress–strain and volumetric interpretations.

CRediT authorship contribution statement

I Wayan Ariyana Basoka: Writing – original draft, Methodology, Investigation, Formal analysis, Data curation, Conceptualization. **Kiyonobu Kasama:** Writing – review & editing, Writing – original draft, Validation, Supervision, Resources, Methodology, Funding acquisition, Conceptualization. **Zentaro Furukawa:** Writing – review & editing, Visualization, Methodology. **Noriyuki Yasufuku:** Writing – review & editing, Validation, Conceptualization. **Ahmad Rifa'i:** Writing – review & editing, Validation.

Acknowledgment

The authors are grateful to the Japanese Government (MEXT) and JICA (Innovative Asia) for supporting the first author during his Ph.D. studies at Kyushu University. We also thank Mr. Yuichi Yahiro and The Ultramicroscopy Research Center Kyushu University for providing technical support.

References

Asadi, M.B., Orense, R.P., Asadi, M.S., Pender, M.J., 2022. A unified approach to link small-strain shear modulus and liquefaction resistance of pumiceous sand. Soils Found. 62 (1). https://doi.org/10.1016/j.sandf.2021.101098.

Basoka, I.W.A., Kasama, K., Furukawa, Z., 2024a. Constant strain rate consolidation testing for pumice sand. Jap. Soc. Civil Eng. Western Branch Res. Present., 431–432

Basoka, I.W.A., Kasama, K., Furukawa, Z., Yasufuku, N., Rifa'i, A., 2024b. Pumice sand behavior on undrained cyclic loading. Japanese Geotech. Soc. Special Publ. 10 (56), 2095–2100. https://doi.org/10.3208/jgssp.v10.OS-45-01.

Basoka, I.W.A., Kasama, K., Furukawa, Z., Yasufuku, N., Rifa'i, A., 2024c. The physical and mechanical properties of single pumice sand particle. GEOMATE J. 26 (115), 73–80. https://doi.org/10.21660/2024.115.g13171.

Bengtsson, M., 2021. Empirical energy and size distribution model for predicting single particle breakage in compression crushing. Min. Eng. 171, 1–9.

Chiaro, G., Kiyota, T., Umar, M., Cappellaro, C., 2022. Earthquake-induced flow-type slope failure in weathered volcanic deposits—a case study: the 16 April 2016 Takanodai Landslide, Japan. Geosciences 12 (11), 1–22. https://doi.org/10.3390/geosciences12110394.

Chindaprasirt, P., Sriyoratch, A., Arngbunta, A., Chetchotisak, P., Jitsangiam, P., Kampala, A., 2022. Estimation of modulus of elasticity of compacted loess soil and lateritic-loess soil from laboratory plate bearing test. Case Stud. Constr. Mater. 16. https://doi.org/10.1016/j.cscm.2021.e00837.

Crosta, G.B., Imposimato, S., Roddeman, D., Chiesa, S., Moia, F., 2005. Small fast-moving flow-like landslides in volcanic deposits: the 2001 Las Colinas Landslide (El Salvador). Eng. Geol. 79 (3–4), 185–214. https://doi.org/10.1016/j.enggeo.2005.01.014.

Fangwei, Y., 2018. Particle breakage and the undrained shear behavior of sands. Int. J. Geomech. 18 (7). https://doi.org/10.1061/(ASCE)GM.1943-5622.0001203 04018079.

Faris, F., Fawu, W., 2014. Investigation of the initiation mechanism of an earthquake-induced landslide during rainfall: a case study of the Tandikat landslide, West Sumatra, Indonesia. Geoenviron. Dis. 1 (4).

Fisher, R.V., 1961. Proposed classification of volcaniclastic sediments and rocks. Bull. Geol. Soc. Am. 72 (9), 1409–1414.

Gibson, A.S., Lafemina, J.P., 1996. Structure of Mineral Surfaces. In: Brady, P.V. (Ed.), . In: Physics and Chemistry of Mineral Surfaces, Vol. 1. CRC Press. https://doi.org/10.1201/9781003068945.

Gupta, A.K., 2016. Effects of particle size and confining pressure on breakage factor of rockfill materials using medium triaxial test. J. Rock Mech. Geotech. Eng. 8 (3), 378–388. https://doi.org/10.1016/j.jrmge.2015.12.005.

Hazarika, H., Sumartini, W.O., Kokusho, T., Kochi, Y., Ishibashi, S., Yamamoto, S., Matsumoto, D., 2019. Investigation on mechanism of landslides during the 2016 Kumamoto earthquake, Japan. Earthquake Geotech. Eng. Protect. Develop. Environ. Constr., 821–832

He, Y., Cai, G., Gao, L., He, H., 2022. Effect of particle size and constraint conditions on single particle strength of carbonate sand. Sensors 22 (3), 1–17. https://doi.org/10.3390/s22030765.

Hosobuchi, M.N., Chigira, M., Lim, C., Komoo, I., 2021. Geological history controlling the debris avalanches of pyroclastic fall deposits induced by the 2009 Padang earthquake, Indonesia: the sequential influences of pumice fall, weathering, and slope undercut. Eng. Geol. 287, 1–15. https://doi.org/10.1016/j.enggeo.2021.106104.

Huang, Q., Zhou, X., Liu, B., 2023. Effect of realistic shape on grain crushing for rounded and angular granular materials. Comput. Geotech. 162. https://doi.org/10.1016/j.compgeo.2023.105659.

Hyodo, M., Tanimizu, H., Yasufuku, N., Murata, H., 1994. Undrained cyclic and monotonic triaxial behaviour of saturated loose sand. Soils Found. 34 (1), 19–32.

Hyodo, M., Wu, Y., Aramaki, N., Nakata, Y., 2016. Undrained monotonic and cyclic shear response and particle crushing of silica sand at low and high pressures. Can. Geotech. J. 54 (2), 207–218. https://doi.org/10.1139/cgj-2016-0212.

Ishihara, K., Tatsuoka, F., Yasuda, S., 1975. Undrained deformation and liquefaction of sand under cyclic stresses. Soils Found. 15 (1), 29–44. https://doi.org/10.3208/sandf1972.15.29.

JGS 0523-2020, 2020. Method for consolidated-undrained triaxial compression test on soils with pore water pressure measurements.

JGS 0524-2020, 2020. Method for consolidated-drained triaxial compression test on soils.

JGS 0530-2020, 2020. Preparation of specimens of coarse granular materials for triaxial tests.

JIS A 1227: 2009, 2009. Test method for one-dimension consolidation properties of soils using constant rate of strain loading.

Kang, X., Xia, Z., Chen, R., Ge, L., Liu, X., 2019. The critical state and steady state of sand: a literature review. Mar. Georesour. Geotechnol. 37, 1–14. https://doi.org/10.1080/1064119X.2018.1534294.

Kasama, K., Furukawa, Z., Yasufuku, N., 2021. Cyclic shear property and seismic runout analysis for pumice fall deposit. Soil Dyn. Earthq. Eng. 143, 1–11. https://doi.org/10.1016/j.soildyn.2021.106588.

Kasama, K., Zen, K., Iwataki, K., 2006. Undrained shear strength of cement-treated soils. Soils Found. 46 (2), 221–232. https://doi.org/10.3208/sandf.46.221.

Khayat, N., 2018. Monotonic behaviour of sand under torsional loading with different confine stress. Int. J. GEOMATE 14 (43), 148–153. https://doi.org/10.21660/2018.43.7359.

Khayat, N., Nazarpour, A., Nasiri, H., Sharma, A.K., 2024. Impact of different temperature conditions on durability and microstructure of clay stabilized. Geomech. Eng. 39 (6), 629–645. https://doi.org/10.12989/gae.2024.39.6.629.

Kobayashi, M., Kuroda, R., Suzuki, K., Fukao, Y., 1991. Models for the Origin of the Pumice Associated with the 1989 Submarine Eruption Off-Ito, Central Honshu, Japan. J. Phys. Earth 39, 21–26.

Kwag, J.M., Ochiai, H., Yasufuku, N., 1999. Yielding stress characteristics of carbonate sand in relation to individual particle fragmentation strength. In: Al-Shafei (Ed.), Engineering for Calcareous Sediments, pp. 79–86.

Mboya, H.A., Makunza, J., Mwishwa, Y.H.B., 2011. Assessment of pumice blocks in comparison to cement sand blocks and burnt blocks 'The Case of Mbeya City - Tanzania. J. Civil Eng. Res. Pract. 8 (1), 43–55. https://doi.org/10.4314/jcerp.v8i1.69524.

McPhie, J., Doyle, M., Allen, R., 1993. Volcanic Texture: a Guide to the Interpretation of Textures in Volcanic Rocks. CODES Key Centre, University of Tasmania.

Mesri, G., Feng, T.W., 2019. Constant rate of strain consolidation testing of soft clays and fibrous peats. In: Canadian Geotechnical Journal, Vol. 56, Number 10. Canadian Science Publishing. pp. 1526–1533. doi: 10.1139/cgj-2018-0259.

Nakata, Y., Kato, Y., Hyodo, M., Hyde, A.F.L., Murata, H., 2001. One-dimensional compression behaviour of uniformly graded sand related to single particle crushing strength. Soils Found. 41 (2), 39–51.

Nasiri, H., Khayat, N., Nazarpour, A., 2024a. Assessing one-year effects of 10 % pumice powder on strength and microstructure of contaminated clay (Case Study: Ahvaz Project, Iran). Case Stud. Constr. Mater. 21. https://doi.org/10.1016/j.cscm.2024.e03892.

Nasiri, H., Khayat, N., Nazarpour, A., 2024b. Utilization of the oil-contaminated soil as a sustainable resource in rural road construction and rehabilitation in oil-producing countries. J. Clean. Prod. 483. https://doi.org/10.1016/j.jclepro.2024.144175.

Nasiri, H., Khayat, N., Nazarpour, A., 2025. Long-term performance and durability of lime-stabilized oil-contaminated soils. Heliyon 11 (2). https://doi.org/10.1016/j.heliyon.2025.e41764.

Oda, M., Koishikawa, I., Higuchi, T., 1978. Experimental Study of Anisotropic Shear Strength of Sand by Plane Strain Test. Soils and Foundations 18 (1), 25–38. https://doi.org/10.3208/sandf1972.18.25.

Orense, R.P., Pender, M.J., 2013. Liquefaction characteristics of crushable pumice sand. Proceedings of the 18th International Conference on Soil Mechanics and Geotechnical Engineering, pp. 1559–1562.

Saito, M., Sagaguchi, K., Komazawa, M., 1997. Geological Map of Japan 1:200,000 (Miyazaki, Kagoshima). Geological Survey of Japan.

Shen, W., Yang, Z., Cao, L., Cao, L., Liu, Y., Yang, H., Lu, Z., Bai, J., 2016. Characterization of manufactured sand: particle shape, surface texture and behavior in concrete. Constr. Build. Mater. 114, 595–601. https://doi.org/10.1016/j.conbuildmat.2016.03.201.

Siebe, C., Salinas, S., Arana-Salinas, L., Macías, J.L., Gardner, J., Bonasia, R., 2017. The ~23,500 y14C BP White Pumice Plinian eruption and associated debris avalanche and Tochimilco lava flow of Popocatépetl volcano, México. J. Volcanol. Geoth. Res. 333–334, 66–95. https://doi.org/10.1016/j.jvolgeores.2017.01.011.

Sumartini, W.O., Hazarika, H., Kokusho, T., Ishibashi, S., Matsumoto, D., Chaudhary, B., 2018. Deformation and failure characteristics of volcanic soil at landslides site due to the 2016 kumamoto earthquake. Int. Associat. Lowland Technol. 19 (4), 237–244 https://www.researchgate.net/publication/326928774.

Tang, C., Zhu, J., Li, Z., Zhu, R., Zhou, Q., Wei, J., He, H., Tao, Q., 2015. Surface chemistry and reactivity of SiO2 polymorphs: a comparative study on α-quartz and α-cristobalite. Appl. Surf. Sci. 355, 1161–1167. https://doi.org/10.1016/j.apsusc.2015.07.214.

Umar, M., Chiaro, G., Kiyota, T., Miyamoto, H., 2018. Monotonic and cyclic undrained behavior of kumamoto-aso pumice by triaxial and torsional shear test. 16th European Conference on Earthquake Engineering.

Umar, M., Kiyota, T., Chiaro, G., Antoine, D., 2019. Undrained monotonic behavior of sand in large strain torsional shear apparatus. Bulletin of ERS 52.

Vranna, A., Tika, T., Papadimitriou, A., 2021. Laboratory investigation into the monotonic and cyclic behaviour of a clean sand stabilised with colloidal silica. Geotechnique. https://doi.org/10.1680/jgeot.18.P.213.

Yoshimoto, N., Hyodo, M., Nakata, Y., Orense, R.P., Hongo, T., Ohnaka, A., 2012. Evaluation of shear strength and mechanical properties of granulated coal ash based on single particle strength. Soils Found. 52 (2), 321–334. https://doi.org/10.1016/j.sandf.2012.02.009.

Zhang, X., Baudet, B.A., Yao, T., 2020. The influence of particle shape and mineralogy on the particle strength, breakage and compressibility. Int. J. Geo-Eng. 11 (1), 1–10. https://doi.org/10.1186/s40703-020-0108-4.